SINGLE-WALLED CARBON NANOTUBE BASED METAMATERIAL ABSORBER FOR SOLAR CELL APPLICATION

A THESIS SUBMITTED TO
THE BOARD OF CAMPUS GRADUATE PROGRAMS
OF MIDDLE EAST TECHNICAL UNIVERSITY
NORTHERN CYPRUS CAMPUS

BY

MADINA OBAIDULLAH

IN PARTIAL FULFILLMENT OF THE REQUIREMENTS
FOR
THE DEGREE OF MASTER OF SCIENCE
IN
SUSTAINABLE ENVIRONMENT AND ENERGY SYSTEMS

June 2017

Approval of the Board of Graduate Programs

_____
Prof. Dr. Oya Yerin-Güneri
Chairperson

I certify that this thesis satisfies all the requirements as a thesis for the degree of Master of Science.

_____
Asst. Prof. Dr. Carter Mandrik
Program Coordinator

This is to certify that we have read this thesis and that in our opinion it is fully adequate, in scope and quality, as a thesis for the degree of Master of Science.

_____
Assoc. Prof. Dr. Cumali Sabah
Supervisor

Examining Committee Members

Assoc. Prof. Dr. Cumali Sabah	Electrical and Electronics Engineering Prog. METU NCC	_____
Assoc. Prof. Dr. Volkan Esat	Mechanical Engineering Prog. METU NCC	_____
Assoc. Prof. Dr. Murat Fahrioğlu	Electrical and Electronics Engineering Prog. METU NCC	_____
Assoc. Prof. Dr. Murat Sönmez	Mechanical Engineering Prog. METU NCC	_____
Assoc. Prof. Dr. Soydan S. Redif	Electrical and Electronics Engineering Dept. EUL	_____

ETHICAL DECLARATION

I hereby declare that all information in this document has been obtained and presented in accordance with academic rules and ethical conduct. I also declare that, as required by these rules and conduct, I have fully cited and referenced all material and results that are not original to this work.

Name, Last name: Madina, Obaidullah

Signature :

ABSTRACT

SINGLE-WALLED CARBON NANOTUBE BASED METAMATERIAL ABSORBER FOR SOLAR CELL APPLICATION

Madina, Obaidullah

M.S., Sustainable Environment, and Energy Systems Program

Advisor: Assoc. Prof. Dr. Cumali Sabah

Co-Advisor: Assoc. Prof. Dr. Volkan Esat

Carbon nanotubes possess superior mechanical and electrical properties such as being lightweight, strong, and flexible; and having high electrical conductivity. Solar cells containing single-walled carbon nanotubes that absorb photons near infrared region have been a focal area of research and development due to their promising characteristics of harvesting light in the long wavelength region, cost effectiveness and performance. Absorption properties of SWNTs are not yet well studied quantitatively, even though their importance is very significant for the new solar technologies. In this thesis, various SWNT based metamaterial absorbers with almost 99% absorption capability have been designed and numerically simulated for the solar cell application. The compact structure and maximum absorption of MTM absorber can provide highly efficient and cost effective solar cell. Novel wide-band, triple-band, and multi-band polarization-insensitive metamaterial absorber structure with semiconducting SWNT as the dielectric layer is proposed to efficiently absorb the incident electromagnetic radiations in a wide-range frequency region. Computed results are verified analytically by interface theory and also with the previously reported MTM absorbers available in the literature as well as with different solver techniques such as FEM and FIT.

Keywords: Single-walled carbon nanotube, metamaterial absorber, wide-band, triple-band, multiband, solar cell

ÖZ

GÜNEŞ PILI UYGULAMALARI IÇIN TEK DUVARLI KARBON NANOTÜPLER
TABANLI META MALZEME SOĞURUCUSU

Madina, Obaidullah
Yüksek Lisans, Sürdürülebilir Çevre ve Enerji Sistemleri Programı
Tez Yöneticisi: Doç. Dr. Cumali Sabah
Ortak Tez Yöneticisi: Doç. Dr. Volkan Esat

Karbon nanotüpler (KNT) hafiflik, sertlik, esneklik, ve yüksek elektriksel iletkenlik gibi üstün mekanik ve elektriksel özelliklere sahiptirler. Tek Duvarlı Karbon Nanotüpler (TDKNT) içeren ve kızılaltı bölgesi civarındaki fotonları emen güneş pilleri uzun dalga boyu bölgesindeki ışımadan faydalanma, ucuz ve yüksek performanslı olma gibi özelliklerinden dolayı popüler bir araştırma ve geliştirme alanıdır. TDKNTler yeni güneş pili teknolojileri için önem arz etmekle beraber soğurma özellikleri nicel olarak yeterince araştırılmamıştır. Bu tezde, güneş pili uygulamaları için %99 soğurma kapasiteli, TDKNT tabanlı çeşitli meta malzeme soğurucular tasarlanmış ve bu soğurucuların numerik olarak simülasyonu gerçekleştirilmiştir. MTM soğurucularının kompakt yapısı ve maksimum soğurma oranları, oldukça yüksek verimli ve uygun maliyetli güneş pillerinin gerçekleşmesini sağlayabilir. Yeni geliştirilmiş geniş-bantlı, üç-bantlı ve çok-bantlı kutuplaşmadan bağımsız, yalıtkan katman olarak yarı iletken TDKNT içeren meta malzeme soğurucular, gelen elektromanyetik radyasyonunu geniş bir frekans aralığında verimli bir şekilde soğurmak için önerilmiştir. Hesaplanmış sonuçlar analitik olarak girişim teorisi ile doğrulanmıştır. Ayrıca literatürde daha önceden yayınlanan MTM soğurucular larla da FEM ve FIT gibi çeşitli çözüm teknikleri kullanılarak doğrulama yapılmıştır.

Anahtar kelimeler: Tek duvarlı karbon nanotüp, meta malzeme soğurucusu, geniş-bant, üç-bant, güneş pili

DEDICATION

To my Beloved Husband, Parents, Grand Parents, in-laws, Siblings.

For their love, belief, and inspiration.

ACKNOWLEDGEMENTS

First, I would be keen on to thank ALLAH for blessing me knowledge and wisdom. It is my pleasure to acknowledge the contribution of others to this work. Not every individual who had an impact on my progress is named explicitly, but I appreciate the help each has given me throughout this journey.

I want to express my appreciation and thankfulness to my advisor Assoc. Prof. Dr. Cumali Sabah and my co-advisor Assoc. Prof. Dr. Volkan Esat for their supervision, direction, and ideas to form the basis of this thesis work. I am indebted to acquire a chance for the research position with them. I would also like to thank all my thesis committee members for their insightful comments in producing this dissertation.

I would also like to reveal immense gratitude to METU-NCC and Chemical Engineering program Co-ordinator Prof. Dr. Türker Gürkan for offering me with an assistantship, which facilitated me exceedingly in funding my MSc, and residing in Northern Cyprus. I would also like to pay my generous respect to all associates of Chemical Engineering for their support.

I would like to acknowledge my friends and colleagues who assisted me in my work. I would like to thank Batuhan Mullah and Bushra Fatima for their continuous support and consultations concerning the enquires and research. Besides, I owe thank to all my friends for their efforts including Humayun Ahmed, Fahad Haneef, Muhammad Saleh Rashid, Samuel Asumadu-Sarkodie, Elham Jahani, Sajed Sadati, and many others helping me in having a good time on the campus.

At last but definitely not the least, I am forever indebted to my husband Obaidullah Mohiuddin, my father Mr. Mahmood Ali, my mother Mrs. Khadija Bano and the rest of my family for their continuous prayers, constant love and encouragement. This would not have been possible without them.

TABLE OF CONTENTS

LIST OF TABLES

LIST OF FIGURES

NOMENCLATURE

$A(\omega)$	Absorption as function of frequency
c	Speed of light (m/sec)
C_h	Chiral vector
CNTs	Carbon nanotubes
DWNT	Double-walled carbon nanotube
E	Electric field (V/m)
ε	Electric permittivity
EM	Electromagnetic
FET	Field effect transistor
FF	Fill factor
H	Magnetic field (Amp/m)
h	Plank's constant
I_{sc}	Short circuit current
ITO	Indium tin oxide
k	Wave number
MTM	Metamaterial
MWNT	Multi-walled carbon nanotube
n	Refractive index
η	Efficiency of solar cell
$R(\omega)$	Reflection as function of frequency
SWNT	Single-walled carbon nanotube
δ	Skin depth
σ	Electrical conductivity (s/m)
$T(\omega)$	Transmission as function of frequency
TDS	Time domain spectroscopy
TE	Transverse electric
TM	Transverse magnetic
TEM	Transverse electromagnetic
UV	Ultraviolet
μ	Magnetic permeability
V_{oc}	Open circuit voltage

ω	Angular frequency (Hz)
z	Impedance

CHAPTER 1

INTRODUCTION

1.1 Motivation

Future technologies will need to incorporate the concept of sustainable and renewable energy consumption to protect the environment and natural resources [1]. The world is now more concerned about finding a solution to improve the solar cell efficiency due to rapid growth in economy and industrialization and the need for generating a green source of energy [2]. Photovoltaic solar cells are semiconducting devices that directly converts the solar radiation into usable electrical energy [3].

Carbon nanotube (CNT) is one of the most promising materials to enhance the efficiency of solar cells [3]. It possesses two to three times higher current conversion density than the commonly used metal conductors [3]. The optimal top contact grid typically covers ~8% of a solar cell that collects no photons thus, no contribution to power production. The capability of having semi-transparent property, CNTs are best suitable as electrical contacts in solar cells to reduce the coverage of metal contacts. CNTs can minimize the blockage of input light and have the greater conductivity than the other semiconducting materials so that it can increase the efficiency of solar cells [3]. CNT based solar cells are the new technologies to improve the system efficiency by increasing the rate of absorption.

To produce energy, most important component of a solar cell is an electrode, which should be transparent and conductive. At present most commonly used and well-known material as an electrode is indium tin oxide (ITO), offers excellent conductivity near 10^3 S cm^{-1} and transparency around 90% at 550 nm [4], [5]. Researchers are working on finding a replacement for ITO due to the shortage of material and separation from zinc and lead ores which makes ITO expensive and inaccessible whereas some of its features restrict its applications such as rigidity and non-solution processability [6]. Many materials are under investigation in which CNTs are considered as the most auspicious substitute showing low resistivity [7], greater flexibility [8], simple fabrication methods [9] and higher specular transmittance [10] in the wide-ranging spectrum from Ultraviolet to Infrared region [11]. The combination of cost and energy efficiency requirement opened the door for researchers to move towards semiconducting single-walled carbon nanotube (SWNTs) as a photon absorber

in the photovoltaic application. Their manufacturing cost significantly reduces due to simple solution processability, scalable fabrication, and purification, which was the drawback in conventional solar cell design [12].

1.2 Carbon Nanotube

CNTs were first invented in 1991 by the Japanese electron microscopist Sumio Iijima [13] and then with his working group; he found out the single-walled carbon nanotubes (SWNTs) in 1993 [14]. Physics community further explored his research and verified the use of CNTs in diverse applications as a result of it's outstanding structural and electrical properties [3]. CNTs are classified into two different types; SWNT and Multi-walled carbon nanotube (MWNT). CNTs are separated into metallic and semiconducting nanotubes according to its chirality, length, and diameter [2]. Mostly MWNTs are metallic, as compared to SWNTs which are only 30% metallic [15]. For instance, armchair CNTs are always metallic whereas chiral and zigzag can be either metallic or semiconducting. In general, SWNTs have much higher electrical conductivity and aspect ratio than the MWNTs compared with the same type, either metallic or semiconducting [16].

Owing to the remarkable electrical, mechanical and electrochemical properties, SWNTs have gathered interest for the nanotechnologies application [17], [18]. The semiconducting SWNT is made up of hexagonal lattice structure consisting of six carbon atoms having movement of a conduction electron in each carbon atom along the σ bonds [19]. Free movement of delocalized π electrons along the SWNT offers higher electrical conductivity to the C-C bond than the copper [20]. SWNTs having smaller diameters [21] have especially fascinated researchers for optical properties as the first optical transition of metallic and semiconducting SWNTs exist in the visible and near infrared region, respectively. SWNTs are direct bandgap semiconductors [22] and highly absorptive materials with a absorption cross section 10^{-18} cm^2 per carbon atom [17].

The way graphene sheet is folded into the layer is called chirality, which determines the electrical properties of CNTs. Chiral vector (C_h) joins the two sites of the graphene which specifies as [20], [23]:

$$C_h = na_1 + ma_2 \tag{1.1}$$

Where a_1 and a_2 are the unit cell vectors of the two-dimensional hexagonal graphene lattice separated by 60^0 angle and the indices *n* and *m* are positive integers that signify the chirality [23]. Each chiral structure of CNT has its optical properties that can change the work function boundary conditions [24]. There are three types of CNT structure; armchair (*n, n*), zigzag (*n, 0*) and chiral (*n, m*) shown in Figure 1-1.

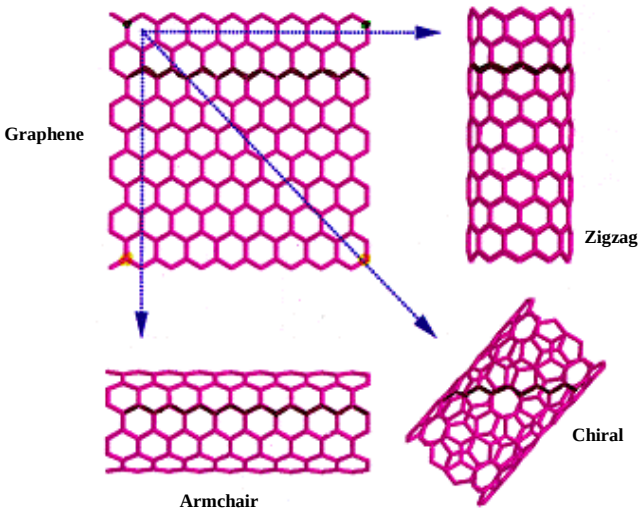

Figure 1-1: Schematics of three types of hexagonal network SWNT structure.

The particular chiral angle for the armchair and zigzag is thirty degree and zero degrees, respectively whereas for the chiral structure it ranges between zero and thirty degrees. The angle of the chiral vector and diameter of SWNTs can be calculated as follows:

$$\theta = \cos^{-1}\frac{n + m/2}{\sqrt{n^2 + nm + m^2}} \tag{1.2}$$

$$d = \frac{\sqrt{3}L\sqrt{n^2 + nm + m^2}}{\pi} \tag{1.3}$$

Where *L* is the bond length or inter-atomic layer thickness, taken as 0.142 nm.

1.3 General Phenomena

Three different phenomena occur within solar cells such as absorption, reflection, and transmission when electromagnetic radiation (sunlight) strikes the surface of the material. Radiations which are absorbed by the material is called absorption, radiations that are

reflected back to the atmosphere is called reflection and the rest which are neither absorbed nor reflected and pass through the material is called transmission. Solar cell performance is significantly disturbed by these three features. The amount of input light reduces caused by photons striking the solar cell enable the reflected light out of the surface, causes more than 30% loss in theoretical efficiency without using an antireflection coating [25]. The conversion efficiency of the solar cells is restricted since they are unable to transform entire solar spectrum radiations. Solar irradiance spectra range is from 100 THz to 1000 THz, which is divided into three sub-frequency regions named as infrared region (100 THz to 400 THz), visible region (400 THz to 750 THz) and ultraviolet region (750 THz to 1000 THz). The performance of solar energy utilization can be increased by decreasing losses of the solar cell, which includes reflection, transmission and recombination losses.

1.4 Photovoltaics (PVs)

The photovoltaic effect implies the generation of electron and hole pairs and their consequent collection at the respective electrodes. Inorganic materials exhibit direct production of free charge from the absorbed photons whereas organic materials require delocalization of excited states by the absorbed photons, which lead to bound-state exciton. These excitons should separate into free charges to transfer to the electrodes [13], [26]. Exciton dissociation can be achieved by potential difference at a junction across polymer and electron acceptor that allows the transfer of an electron to the acceptor while leaving the holes to be transported to the polymer, called photoinduced charge transfer [27]. Compared to organic and inorganic photovoltaic material, SWNTs possess excellent exciton, absorption cross section and free carrier diffusivity, and mobility. So far polymer solar cells based on SWNTs utilizing individual, mixed semiconducting and metal chiralities with 0.01% to 1.7% external quantum efficiency (EQE) have been established [12]. The purpose of the polymer is to work as an isolating agent or as primary layer element that can only improve the performance of solar cells at small scale and require highly controlled environment due to increased photo-instability. However, CNTs are highly stable in air and absorbs in the near infrared range which leads to the development of the polymer free solar cells [28].

1.5 PVs with CNTs

It has exposed recently that implementation of carbon nanotubes in photovoltaic solar cells as an active element can increase the free carrier response so that next generation solar cell

efficiency and functionality can be improved through CNTs [29]. Carbon nanotubes possess extraordinary properties being a promising material to harvest sunlight in photovoltaic solar cells. It offers faster exciton and efficient charge transfer which has been the drawback in the polymers [30]. Several groups have studied nanotube composites using conjugated polymer PPV (polyphenylene vinylene) and its derivatives. The aim of the addition of carbon nanotube to the polymer is to enhance the electrical conductivity. It has been observed that electrical conductivity of polymer improved by eight-fold with nanotube without degrading the optical properties [13]. It has also been validated from electrical conductivity data that by the addition of 0.1 and 0.2% w/w SWNT into the polymer can increase the electrical conductivity by 10^5 [27].

High surface area (1600 m^2/g) and superior electrical properties of SWNTs make them highly efficient materials to fabricate organic solar cells. Carbon nanotubes can be used in two ways; one is in the electrode to obtain better cell performance, improve charge separation, and enhance the roughness factor; and the second is the alignment of semiconducting CNTs as an active material in the photoactive layer to increase the short-circuit photocurrent (I_{sc}), density and fill-factor (FF). Random orientation of nanotubes results in multiple crosses of electrons through the boundaries and hurdles in charge transportation which leads to a decrease in the solar cell efficiency [31].

The semiconducting SWNTs as an active material absorb sunlight and then convert it into useful form of electrical energy by generation of electron and hole pairs [32]. Inefficient conversion of solar energy occurs due to the losses within and out of the solar cell including loss in metallic part caused by the generation of heat [33]. Thickness of the active material is also one of the important parameters. Increase in depth of the active material causes recombination of previously created electron hole pairs. As a nanomaterial, carbon nanotubes prevent these kind of losses within the solar cell [34].

1.6 Optoelectronic Properties of CNTs

CNTs networks are made-up of metal-metal, semiconductor-semiconductor and semiconductor-metal, junctions. It is necessary to investigate the optical and electrical properties accurately concerning the application in nanoelectronics [35]. The characteristics of Electromagnetic properties such as electric permittivity and the magnetic permeability have a huge influence on the interaction between electromagnetic radiation and material. They are

necessary parameters to evaluate the propagation of electromagnetic waves in the medium due to the presence in the dispersion equation [36], [3]. The resistance encountered between the electric field, and the medium is called electric permittivity whereas the behavior of the material in reaction to an applied magnetic field is called magnetic permeability [3].

Three different types of material exist in electronics; insulator, semiconductor, and conductor. These materials are categorized by their conductivity level known as energy band structure [37], [3]. The only energy band that is of concern in the solar cell is the valence and conduction band distinct from void space. Valence band is the outermost energy shell of an atom or the lowest energy level, which is partly occupied by electrons, while the highest energy level and usually empty is the conduction band. An electron in the valence band acquires an energy same or greater than the gap between the conduction and valence band is called bandgap or forbidden band. These electrons then move into the conduction band and break away to form free electrons in the material [3], [38]. Materials are highly reliant on the bandgap to conduct electricity. In conductors, electrons do not require external energy to travel from valence band to conduction band as both bands overlap. Whereas semiconductors need some energy due to the smaller bandgap, which enables them to act as an insulator. Besides, insulators have larger bandgap that entail more energy to excite an electron [39], [3].

All materials have different bandgap and electrical properties that convert the only portion of solar light into electrical energy due to the properties of the solar cell. The bandgap decides the amount of energy required to produce an electron and hole pair. If the photon has less energy than bandgap, then it will not excite the electron and waste all energy passing by the material. It has been shown that materials that have lower bandgaps are more capable of utilizing a broad spectrum of photons than the materials with larger bandgap. Photon's energy is also reliant on the wavelength calculated as

$$E = \frac{1.24}{\lambda} \tag{1.4}$$

where E is the photon energy in eV and λ is the photon's wavelength in μm.

There have been a substantial number of studies on the electrical properties of the carbon nanotube, but still, it is complex to draw an exact conclusion of electrical conductivity from these findings since the results are varying widely between 1 to 10 % [40]. It is observed experimentally by Ebbeser et al. in both semiconducting and metallic nanotubes that electrical

properties vary significantly from tube to tube [41]. The electrical conductivity of CNTs and their composites with polymers are highly dependent on several parameters such as chirality, % purity, length, and diameter of the tube [35].

1.7 Application of CNTs

Prospect of using CNTs has been widely investigated for many applications owing to their distinctive mechanical, electrical and field emission properties. Companies like IBM, Fujitsu, and many other research organizations have built prototype devices using semiconducting carbon nanotubes such as CNT field effect transistors (FETs), and nanoantenna. [23], [42].

Amongst all potential transistor technologies, CNT-FET is the most competitive one having distinguishable qualities. It exhibits four times higher current capability and transconductance than the Si-MOSFET (Metal Oxide Semiconductor Field Effect Transistor). CNT-FET was stated as back-gated in the past. However, it has been discovered that approximately ten times improvement can be achieved in the transconductance of CNT-FET [42].

There are lots of applications reported in the literature for microwave and terahertz regions ranging from $3x10^8$ to $3x10^{11}$ Hz and $3x10^{11}$ to $3x10^{12}$ Hz, respectively. Nougaret et al. [43] employed Semiconducting SWNTs in back-gated CNT-FET with frequency up to 80 GHz are proposed that, if parasitics can be neglected, up to 80 THz frequency can be accomplished. Sazonova et al. [44] established tunable CNT electromechanical resonators in RF mixer configuration. Hanson has demonstrated characteristics of CNT dipole antenna system up to THz frequency region. CNTs possess 100 times smaller wave velocity than free space so that CNT antenna have the ability to resonate with low frequency than copper wire [44].

Urgent need of environment-friendly and sustainable energy production has enabled the use of CNTs in fuel cell applications as an alternative catalyst due to higher surface area with a significant porosity, which allows uniform deposition of catalyst on CNTs to enable catalyst exploitation. Furthermore, compared with the carbon black material, CNTs are enriched in terms of electrochemical stability with superior electrical conductivity and highly resistive to electrochemical oxidation resulting in enhanced performance regarding fuel conversion efficiency [18].

Supercapacitors based on CNT electrode is best suitable for applications entail that an enormous amount of power capability and storage than batteries and capacitors, for instance,

portable electronic devices, digital communication, and hybrid electric vehicles to produce rapid acceleration, high cycle efficiency and storing of electrical energy. The capacitance and power density of SWNT are 180 F/g and 20 kW kg^{-1} (at an energy density of approximately 7 W-h/kg) respectively which is very attractive because performance can enhance by interchanging bundled SWNTs with unbundled ones [45], [46]. The high conductivity of CNTs are revealed to have improved specific capacitance and cycle efficiency as an electrode for electrochemical super-capacitor when deposited with conducting polymer and metal oxide through the effect of faradaic (pseudocapacitance). Also, integration of CNTs leads to enhanced mechanical strength and cycle stability of an electrode [18].

The use of CNTs as an alternative anode in lithium ion batteries is one of the potential applications due to the high energy density and reversible storing size at a high level of discharging. The optimum reversible size of purified mechanically milled SWNTs is 1000 mA-h/g which is significantly higher when compared with graphite 372 mA-h/g [45], [47]. However, observation of nonexistent voltage peak, huge irreversible capacities, and hysteresis among charge and discharge have restricted its application as an energy storage material as compared to other resisting materials [18].

Industries and educational investigators are focusing on electronic devices that use CNTs as field emission electron such as lamps, X-rays, microwave and flat panel display. Smaller radius and a greater length of CNTs enabled higher local field in response to applied potential between coated CNTs surface and an anode which result in a shift of an electron from nanotube tip to the vacuum. Then these electrons are directed to the anode by an electric field to harvest light from phosphor for flat plate display application [45]. Fabrication of nanotube field emitting surfaces are very simple through the screen printing method and last long in the adequate vacuum of 10^{-8} torr as compared to tungsten and molybdenum, which are challenging to manufacture and require 10^{-10} vacuum [45], [48].

CHAPTER 2

LITERATURE REVIEW

CNTs have been widely investigated since discovered due to their distinctive mechanical and electrical properties and considered as a potential constituent in the nanoscale circuits [15]. Presently, solar cell technologies have great importance in military and civilian sectors due to the generation of renewable source of energy in remote locations and most economical solution [3]. The cost of solar cell installed per watt has been decreasing every year by 5-6 % since last decade due to advancement in technology. Worldwide installation of the photovoltaic market has achieved the highest level up to 1460 MW in 2005 with an annual expansion of 34%.

The first crystalline silicon-based solar cell with the lowest 4% efficiency has been created in 1954. However, the efficiency of the silicon heterojunction solar cells now reached up to 25% [49]. Absorption enhancement of incident radiation leads to an increase in the thickness of silicon solar cell, which means wastage of material and the increase in cost. Thus, amorphous silicon solar cell is fabricated to reduce the film thickness of the solar cell with an efficiency of 13% [50]. Three generation of solar cells has been introduced. First, polycrystalline silicon-based solar cells are manufactured, which are known as generation I. Second generation was introduced to improve the efficiency, based on the thinner material of various compositions deposited on the cheaper substrate. Third generation solar cells comprise of multi-junction and intermediate band with the highest efficiency of 44.7% till now [51]. The summary of all generations of solar cells is shown in Figure 2-1. These types of solar cells can reach high efficiencies, but their production cost is very high which restrict them for economical applications [52]. Therefore, it appears to be challenging but an essential task to research and generate alternative materials. Different types of nanostructures including nano-composites, quantum wells, nanoparticles, and nanotubes have been incorporated to make efficient and cost-effective solar cells [50]. Among those, CNTs are the potential organic material to fulfill this challenge, which can combine different chiralities and bandgaps to get a continuous response over a wide spectrum. Early endeavors were made to use SWNTs as a transparent conductor in PV solar cells, beginning in 2006 with organic PV with power conversion efficiency (PCE) of approximately 1.5% [53]. Afterward, in 2007 SWNT was incorporated in CdTe solar cells as semi-transparent back contact and achieved 12.4% [54] and in the same year SWNT was substituted with ZnO transparent conductor in CuIn-GaSe solar cell and

accomplished 13% PCE [55]. Several types of research have been done in the following years to understand and manipulate the various factors of SWNTs to examine the electrical and optical properties.

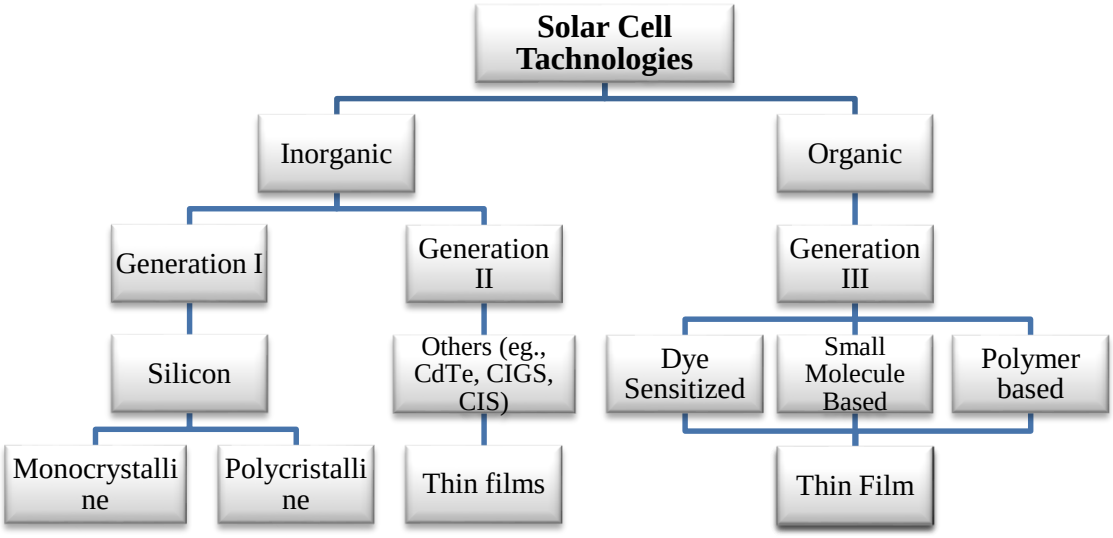

Figure 2-1: Categories of photovoltaic technologies.

2.1. Gaps in literature

Various computational and experimental researches have been done on the CNT based solar cell especially on SWNT since emergence. Some of which are discussed in this chapter to highlight the requirement for more research in this highly challenging area.

Electromagnetic properties such as electric permittivity is the ability to resist the electric field whereas the magnetic permeability is the capacity to create an internal field in the magnetic field [56]. Electromagnetic properties of SWNT can be modified by optimizing geometry, morphology, orientation and chirality. Absorption coefficient A(ω) as a function of frequency can be determined by two basic parameters, reflection R(ω) and transmission T(ω) that can be calculated as,

$$A(\omega) = 1 - R(\omega) - T(\omega) \quad (2.1)$$

Transmission coefficient can be eliminated using two methods. Firstly, use a combination of multiple layers in CNT solar cell design to reduce transmission. Secondly, apply thick metal

ground plane in the CNT absorber so that transmitted wave will be reflected back to eliminate transmission. After removing the transmission losses, the only threat left to the accomplishment of perfect absorption is the reflection. Reflection can be controlled by geometrical parameters, which modify the structural properties such as of electric permittivity and magnetic permeability and adjust the structural impedance. Perfect absorption occurs when the absorption rate of material is very high with lower rate of reflection, which means that the impedance of the material matches to the impedance of free space [57]. In practical applications, it is hard to characterize the individual CNT in the THz region due to complexity in fixture fabrication and large impedance mismatch. Therefore, characterization of the large group of the nanotube is easier for transmission and reflection measurement [58]. However, most of the experimental studies reported only reflection or only transmission neglecting the rest of the information; thus, magnetic permeability had been assumed to be unity to extract the permittivity [15]. In their study; Liang et al. mentioned that impedance mismatch between air and substrate causes multiple reflections under CNT film/layer which impede the major pulse and emerges in the transmission results known as Fabry-Perot effect. So, multiple reflections should be considered while computing the transmission coefficient [58].

Several materials are transparent in THz radiation due to having the property of being opaque to visible and infrared. Complications in numerical transformation process limit the absorption spectrum in the microwave and far-infrared region. Characterization of optical and electrical properties using TDS in THz region at low and high frequencies shows that polarized aligned SWNTs are strongly anisotropic whereas non-aligned SWNTs show isotropic behavior. [35] Microwave and infrared properties of SWNTs had been studied previously. However, the carbon nanotube has significant absorption in the optical region, which is not examined in detail, yet.

The main component of the solar cell is the absorber so the main objective of this thesis is to design the perfect SWNT absorber as an active material to analyze the absorption properties in the THz region. Research includes geometry optimization, morphology, orientation, and chirality of carbon nanotube to achieve a superior absorber; thus, improve the efficiency of solar cell. A detailed literature review based on analytical modeling, computational modeling and experiment has been presented in the next sections.

2.2. Literature review on experimental studies

Varied experimental studies have been performed to improve the efficiency of CNT based solar cells. CNTs have been incorporated in many types of PV's such as in PV wires as an electrode [59], composite with polymers [26], replacement of ITO [4], to eliminate polymer [28], in dye synthesized [60] and organic photovoltaic solar cells [31]. Kymakis et al. [26] experimentally studied the first SWNT-based solar cell to investigate the optical and electrical properties of the SWNTs/conjugated polymer composite photovoltaic device. They used indium tin oxide as an electrode and deposited the thin SWNT polymer composite film on it and compared their results with pristine polymer diodes which showed significant improvement in the performance of SWNT/P3OT photovoltaic and achieved the short-circuit photocurrent (I_{sc}) two order magnitudes greater than the pristine device. However, the open circuit voltage (V_{oc}) and the fill-factor (FF) increased from 0.7-0.9 V and 0.3 to 0.4 respectively. Also they found that most of the incident light (> 60%) was absorbed in the region of 2.2 to 2.8 eV. Photovoltaic properties improved by the junctions between the polymer matrix and SWNT/polymer which provide a continuous passage for energetic transportation electrons towards negative electrode [26]. Landi et al. [27] constructed a photovoltaic device based on 1% w/w purified SWNTs and regioregular poly (3-octylthiophene) composite. SWNTs were fabricated using pulse-laser vaporization technique. The deposition of SWNT-P3OT composite solution onto the indium-tin oxide coated with polyethylene terephthalate has been done followed by aluminum contact. Authors claimed that electrical conductivity could enhance up to approximately 10^5 by the addition of 0.1 and 0.2% w/w SWNT into the composite. The rate of absorption and electrical conductivity increases with increase in the percentage of SWNT doping into the composite resulting in an improvement in carrier shuttle and I_{sc}. Even at very low SWNT doping, significant improvement observed in the absorption in the optical and infrared region. The measured V_{oc} and I_{sc} were 0.98 Volt and 0.12 m-A/cm^2, respectively [27].

In another experimental study carried out by Chen et al., they fabricated organic solar cell using polymer and highly aligned nanotube fiber composite and compared the results with the traditional rigid plate based solar cells. It has been shown that due to highly aligned nanotubes which possess extraordinary electrical properties, solar cell accomplished large I_{sc} of 10.3 m-A/cm^2 with 2.6% maximum power conversion efficiency and other photo-response characteristics such as V_{oc} and FF which are 0.47 Volt and 0.45, respectively [31]. After that Jain et al. incorporated purified (6, 5) SWNTs layered with C_{60} to build polymer free solar

cell near infrared region. They found the I_{sc} = 0.81 m-A/cm^2, V_{oc} = 0.33 Volt, FF = 0.37 and efficiency = 0.10%. The efficiency achieved by eliminating polymer is comparable to the polymer-based solar cells. They also made the device using 20% (6, 4) and 80% (6, 5) SWNTs by weight and observed 30% reduction in PCE as compared to purified 100% (6, 5) SWNTs. This is because electrons and holes trapped within the mixed chiral nanotube film provide exciton recombination [28]. It is essential to separate different chirality SWNTs and combine with semiconductors in order to facilitate full exploitation potential of SWNTs in the photodetector and efficient exciton dissociation [61]. Absorption calculations on a group of SWNTs have to face heterogeneity issues because of the synthesis method. It's hard to measure the exact amount of specific SWNT's absorption due to the presence of ensembles of multiple chirality nanotubes, length and synthesis impurities [62]. CNTs also have been employed as a substitute of ITO in organic solar cells since it is easy to deposit on polymer substrate at a normal state. To build a conductive and transparent polymer, selection of primary and secondary dopants are very crucial for control chemical doping [4]. Salvatierra et al. constructed an organic solar cell with CNTs as an electrode to replace ITO. CNTs exhibit high resistance among each other; therefore, polyaniline derivative (PANI) is layered by interfacial polymerization between them to decrease the resistance, ultimately reducing percolation threshold. Two steps have been encountered to improve the film parameters, secondary doping of polyaniline and reduction in CNTs diameter. It is experimentally evident that the larger diameter (70nm) of CNTs exhibit inhomogeneous and highly dispersed film which reduces the transparency and conductivity, so that CNTs should be selected with a smaller diameter (10nm) to produce the high-quality film. Authors claim that increased concentration of CNTs in the film enhances the rate of absorption and also varies the roughness. PANI: CNT5 observed to have the (12 nm) minimum roughness level, besides the conductivity, transmittance and resistance of this film found to be 22.1 Scm^{-1}, 89.4 %, and 85 kΩ at 550 nm, respectively. PANI/CNT7 and PANI/CNT10 have also been investigated, but they exhibit lower conductivities caused by interference during polymer formation process [4].

Chen et al. developed photovoltaic wires by employing CNT fiber as an electrode which supplies efficient charge separation and electron transport. CNT has twisted with TiO_2 which has aligned onto the titanium wire by electrochemical anodic oxidation with an active layer of poly (3-hexyl-2,5-thiophene) (P3HT) and 6,6-phenyl-C_{71}butyric acid methyl ester ($PC_{70}BM$). Anodic oxidation is highly dependent on time as it can change the thickness of TiO_2, which has a significant effect on the performance of the polymer wire. Authors did

experiment on different anodizing times and observed that I_{sc} and efficiency increased from 0.5 to 0.98 m-A/cm^2 and 0.06 to 0.15% respectively when the anodic oxidation time increased from 1 to 5 min. The V_{oc}, I_{sc}, FF, and efficiency of were found to be 0.42 V, 0.98 m-A/cm^2, 0.36, and 0.15%, respectively, at the anodizing time of 5 min. [59]

2.3. Literature review on Analytical modeling

In nanotube solar cell devices, optoelectronic, complex dynamics and design parameters including nanotube chirality, alignment, density, thickness, length, and diameter are important variables that can impede experimental research and design intuition. Some approaches contradict with the optimum alignment of the nanotube. Darin et al. [12] developed a mathematical model to describe the characteristics of the solar cell design such as nanotube density, chirality, length, film thickness, and orientation for planner heterojunction devices. Authors adopted the basic physics of SWNTs to derive the mathematical equations. To set the SWNTs parameters randomly, they assumed macroscopic homogeneity. This research depicted that vertically aligned nanotube with densities more than 3% of the closed packed density is favored to increase the charge transport. Moreover, 10 to 100 times better performance has been accomplished with a vertical orientation and density greater than 10% of the closed packed. However, there were some drawbacks in the system; at the interface of the nanotube (mainly with different chirality) the equilibrium charge transfer has not been taken into account and photo-luminance, and Rayleigh were also neglected [12].

Fourier transformed infrared (FTIR) and microwave spectroscopy has some limitations in the current-voltage measurement. For instance, FTIR requires complicated process calculations like Kramer-Kronig relationship and microwave is not applicable in the higher GHz and THz range. Therefore in the THz region, TDS is validated for the determination of frequency dependent electrical and optical properties since it acquires a high signal to noise ratio (5000:1) to yield more precise results [16]. Maenf et al. [16] performed terahertz characterization of double-walled CNTs (DWNT) and compared them with SWNTs using THz-TDS in the frequency range of 0.2 to 2.5 THz. The power absorption and refractive index of DWNTs are much smaller than the SWNTs. Moreover, SWNTs possess 3 to 4 time greater conductivity than the DWCNTs [16]. Wang et al. [15] used vector network analyzer (VNA) to evaluate the scattering parameters of MWNT film comprising of arbitrarily oriented nanotubes in the frequency range of 8-50 GHz. Effective complex permeability and permittivity were computed by developing analytical equations and verified by using Ansoft's

high-frequency structure simulator. To eliminate the impact of air and to acquire more accurate properties, the effective medium theory was implemented. From the uncertainty analysis, it has been found that ambiguity related to the reflection coefficient has much more effect on the results as compared to the change of transmission coefficient. A minor discrepancy in the reflection coefficient leads to major transformation on the materials parameters while the impact of transmission coefficient is not sensitive. To find out the relative permeability and permittivity of the CNTs authors employed the Nicolson Rose Weir technique. Drude-Lorentz model technique has been implemented, which provided an appropriate fitting in the frequency range of 8 to 50 GHz in order to get more intuition into the nanotube characteristics and produce mathematical relationship for future technologies. The estimated dielectric constant $\varepsilon'$of CNT film has been found from 250 to 700 corresponding to the resulting conductivity range of 810 to 1500 S/m [15]. Another study carried out by Wu et al.[63] continued in the path of the aforementioned research in the microwave region from 8 to 50 GHz that experimentally performed the reflection and transmission analysis in the frequency range of 50 - 370 GHz to calculate the refractive index and wave impedance of the MWNTs using terahertz-TDS. The electromagnetic properties, dielectric-permittivity, and magnetic-permeability have been calculated as,

$$\varepsilon = \frac{n}{z} \tag{2.2}$$

$$\mu = n \times z \tag{2.3}$$

The measured μ was increased with increase in frequency from -1 to 8 whereas ε was decreased from 600 to 20 as frequency increased. They also used Drude-Lorentz model to have more physical intuitions of the material properties. Table 2-1 shows the fitting parameters of the model for MWNTs in the frequency range of 8 - 50 GHz and 50 - 370 GHz. Drude-Lorentz (D-L) model is described as follows:

$$\varepsilon = \varepsilon_c - \frac{\omega_p^2}{\omega(\omega - j\Gamma)} + \frac{\omega_{p1}^2}{-\omega^2 + j\omega\Gamma_1 + \omega_1^2} \tag{2.4}$$

Table 2-1 Drude-Lorentz model-parameters for MWNT

Parameters	Explanation	8-50 GHz (rad/s)	50-370 GHz (rad/s)
ε_c	Constant independent of frequency	3.52	60
ω_p	Plasma frequency	1.5 x 10^{11}	7.49 x 10^{12}
Γ	Relaxation rate of electron	1.1 x 10^{13}	6.46 x 10^{11}
ω_{p1}	Oscillation strength	6.0 x 10^{13}	1.15 x 10^{14}
ω_1	Central frequency of the resonance	3.6 x 10^{11}	4.20 x 10^{12}
Γ_1	Spectral width of the resonance	2.4x10^{13}	8.10 x 10^{13}

Characteristics of perpendicular and parallel aligned SWNTs using time domain spectroscopy (TDS) has been measured from 0.2 to 2 THz by Jeon et al. [64] in far-infrared region. Since at low frequencies, conductivity does not ensure the simple Drude model, combined Maxwell-Garnett (M-G) with D-L model was established to describe the CNTs embedded in an effective dielectric air media integrating both metallic and semiconducting nanotubes. As a result, most of the conductivity was donated from the localized photons arising from doped semiconducting nanotubes. The real conductivity was shown to bring improvement with an increase in the frequency. Alignment of SWNTs did not show a significant effect on the electric permittivity [64]. Drude-Lorentz absorption parameters are shown in Table 2-2. Dadrasnia et al. [35] performed an analysis for non-aligned SWNTs and MWNTs in the frequency range of 0.1 to 2 THz. They also used combined M-G with D-L model and compared the results for conductivity claiming that SWNTs have two times greater conductivity than the MWNTs because of the ease of carrier mobility and low surface defects in SWNTs. This combined model for calculating effective permittivity is only applicable for the frequency of ~20 THz, beyond which the effective medium theory is not valid. The D-L model parameters are illustrated in Table 2-2 [35].

Table 2-2 Drude-Lorentz model parameters for aligned and non-aligned SWNT [35].

Frequency Range	Alignment	ε_c (THz)	ω_p (THz)	Γ (THz)	ω_{p1} (THz)	ω_1 (THz)	Γ_1 (THz)
0.2-2 THz	Parallel	3.24	5.40	1.17	6.19	2.40	4.50
	Perpendicular	3.24	5.65	1.60	4.32	2.32	2.96
0.1-2 THz	Non-aligned	8.9	30	10.2	23.65	2.16	9.5

2.4. Computational Modelling

Rahman et al. simulated the CNTFET array as a photovoltaic component to maximize absorption rate using COMSOL Multiphysics software. Air surrounded the chiral (16, 0) CNT in a simulation box with an incident of solar radiations from the top. Bottom surface was decided to be transparent for the scattering and incoming waves with all incident angles. Boundary conditions of the side walls were defined as perfect electric and magnetic conductor. Two different orientations of CNT were simulated; perpendicular, and parallel. The existence of CNT resulted in the alteration of the electromagnetic field, and also in the power absorption (P). The power absorption were found to be 5.16 x 10^{-14} Watt. After calculating the power absorption, rate of optical power generation (G_{op}) was calculated as follows:

$$G_{op} = \eta \times \frac{P}{h\,\omega} \times \frac{1}{L} \tag{2.5}$$

where quantum efficiency (η) was taken 10% with 1000 nm length (L) of carbon nanotube and ω is the frequency of incident solar radiations. Tree fractal topology presented 67.4% improvement in power absorption as compared to parallel array [50]. Adam et al. modelled the heterogeneous CNTs with GaAs solar cell in Silvaco ATLAS software. To reduce losses from the top contact due to charge carrier, they used a CNT layer as top contact. They found that current gathered at the top layer and moved to the contact through smaller resistance minimizes the voltage drop resulting in maximum power output and increase in the efficiency of the solar cell, whereas the only small portion of incident light is lost as transmission from the CNT layer. The flow of current in the top contact grid lines causes losses that can be minimized using wider CNT top layer due to less shading; thus, the maximum possible overall efficiency of a solar cell may be achieved [3].

Elwi et al. carried out a numerical study using finite integration techniques to investigate the electromagnetic properties of dipole antenna system based on (10, 10) armchair SWNT in the near infrared region from 400 THz to 625 THz. The author made the original hexagonal structure of nanotube in CST MICROWAVE STUDIO and compared the results with the rod and tubular nanotube structure. The combination of carbon atoms in hexagonal structure offers highly extensive potential pathways for electron's motion as compared to single pathway provided by hollow and solid cylindrical geometries thus indicated vast differences in resonant frequency, bandwidth, and radiation efficiencies. These differences are attributed

to change in current distribution and provide an efficient pathway to pass the current resulting maximum in current density in hexagonal structure because of the effective length of the structure [20].

CHAPTER 3

DESIGN AND ANALYSIS OF PERFECT CNT ABSORBER

In this chapter, approaches that have been considered in designing and analysis of the CNT absorber in order to improve the accuracy of the results are explained in detail. The initial step for the designing of the CNT absorber is to find the frequency dependent material parameters such as permeability and permittivity in the frequency range of interest for the different chiral SWNTs. For this purpose, experimental or measured scattering parameters are required for every chiral SWNT. Scattering parameters are also known as S-parameters, which includes the reflection (S_{11}) and transmission (S_{21}) coefficients. An algorithm based on Nicolson-Rose-Weir (NRW) technique is established on MATLAB to acquire the effective permeability and permittivity of the single-walled carbon nanotube at different chiralities. The SWNT chiralities that has taken into consideration are (5,4), (6,4), (6,5), (7,5), (9,4) and (10,3) [28], [30], [65], [66]. The selection of chiralities is based on the availability of scattering parameters data in the literature in the frequency ranges between 100 THz to 1000 THz. The permeability and permittivity of these Chiral SWNT can be calculated using the following algorithm.

3.1 Permeability and permittivity retrieval

The NRW utilizes S-parameters to retrieve the complex permeability and permittivity of the SWNT. It is a common approach in the literature for parameter extraction using measured or simulated S-parameters by using the following procedure. The s-parameters S_{11} and S_{21} are related to refractive index (n) and wave impedance (z), can be expressed as,

$$S_{11} = \frac{R_{01}(1 - e^{i2nk_0d})}{1 - R_{01}^2 e^{i2nk_0d}} \tag{3.1}$$

$$S_{21} = \frac{(1 - R_{01}^2)e^{ink_0d})}{1 - R_{01}^2 e^{i2nk_0d}} \tag{3.2}$$

where $R_{01} = \frac{z-1}{z+1}$, κ_0 denotes the free-space wave number, d is the thickness of the CNT and $n = n' - in''$ is the complex index of refraction of the material. The complex wave impedance $z = z' - iz''$ and transmission coefficient (ξ) can be calculated as,

$$z = \pm\sqrt{\frac{(1 + S_{11})^2 - S_{21}^2}{(1 - S_{11})^2 - S_{21}^2}} \tag{3.3}$$

$$\xi = e^{in\kappa_0 d} = X \pm i\sqrt{1 - X^2} \tag{3.4}$$

$$X = \frac{1}{2S_{21}}\left(1 - S_{11}^2 + S_{21}^2\right) \tag{3.5}$$

The positive and negative sign in the equation (3.3) and (3.4) can be determined by manipulating the requirement $z' and\ n''$ should be greater than or equal to zero. The refractive index (n) can be calculated from equation (3.6) after calculating the natural log of $e^{in\kappa_0 d}$ as,

$$n = n' + in'' = \frac{\left[Im\left[\ln\left(e^{in\kappa_0 d}\right)\right] + 2m\pi\right]}{\kappa_0 d} - i\frac{Re\left[\ln(e^{in\kappa_0 d})\right]}{\kappa_0 d} \tag{3.6}$$

$$n' = \frac{Im\left[\ln\left(e^{in\kappa_0 d}\right)\right]}{\kappa_0 d} + \frac{2m\pi}{\kappa_0 d} = n_0' + \frac{2m\pi}{\kappa_0 d} \tag{3.7}$$

$$n'' = -\frac{1}{\kappa_0 d} Re\left[\ln\left(e^{in\kappa_0 d}\right)\right] \tag{3.8}$$

Where m is any number. Evidently, n'' is easily calculated, whereas, n' is probmematic due to the branching of the logarithm function and has infinite number of possibilities. As suggested in the fcenterliterature, if we know the imaginary part of any material parameter then the real part can be calculated by using Kramers-Kronig (K-K) relation and vice versa. Therefore, K-K relation is applied to determine n' as,

$$n'^{k-k}(\omega') = 1 + \frac{2}{\pi} P \int_0^\infty \frac{\omega \times n''(\omega)}{\omega^2 - \omega'^2} d\omega \tag{3.9}$$

where P is the principal value of integral. The integral in equation (3.9) can be solved numerically as,

$$n'^{k-k}(\omega_i) = 1 + \frac{\Delta\omega}{\pi}\left(\sum_{j=1}^{i-2} \psi_{i,j} + \sum_{j=i+1}^{N-1} \psi_{i,j}\right) \tag{3.10}$$

$$\psi_{i,j} = \frac{\omega_j \times n''(\omega_j)}{\omega_j^2 - \omega_i^2} + \frac{\omega_{j+1} \times n''(\omega_{j+1})}{\omega_{j+1}^2 - \omega_i^2} \tag{3.11}$$

Once n'^{k-k} is predicted from the K-K relation, it can be substituted in equation (3.7) to calculate the branch number (m) as,

$$m' = Round\left[\left(n'^{k-k} - n_0'\right)\frac{\kappa_0 d}{2\pi}\right] \tag{3.12}$$

The Round-function is applied to show that *m'* is an number closest to $\left(n'^{k-k} - n_0'\right)\frac{\kappa_0 d}{2\pi}$ .The actual real part of the refractive index is then calculated after putting the value of *m'* in equation (3.7). Afterward, the relative permittivity (ε) and permeability (μ) parameters are calculated as,

$$\mu = nz \tag{3.13}$$

$$\varepsilon = \frac{n}{z} \tag{3.14}$$

This algorithm is developed on the MATLAB and utilized for all chiralities of CNT under consideration. To make sure the algorithm is working correctly and the results are accurate, the S-parameters plots of the known permeability and permittivity for the CNT film in [67] are digitized and used in the algorithm and results are compared to ensure the accuracy of the developed model.

3.2 Design Methodology

After calculating the frequency dependent permeability (both real and imaginary) and permittivity (both real and imaginary) of SWNT for the different chiralities listed above are introduced into the simulation software. In this thesis, Finite Integration technique based software CST MICROWAVE Studio is used for the designing and analysis of the proposed CNT-based absorber. Designing of a perfect absorber requires some specifications with respect to the selection of basement material and the dimensions. To obtain the accurate and reliable results, it is necessary to ensure correctness of the modeling and analyzation. In this chapter, the analyzing and modeling techniques and approaches are discussed briefly.

In order to eliminate the transmission losses, ground plane substrate material has to be selected which should be metallic. Ground plane made of metallic material prevents the escape of electromagnetic radiation from the bottom by reflecting back to the semiconducting layer instead. The EM properties of the materials are reliant on the frequency so that permittivity, permeability, conductivity and refractive index as a function of frequency are defined by using empirical data and dispersion model like Drude model.

After the selection of the bottom substrate material, one of the most important steps to designing a perfect absorber is a determination of the geometrical dimensions. For carbon nanotube, length, chirality, diameter, and orientation are the most important parameters. However, for the basement metallic plate, thickness of the material is crucial. The thickness of the basement metallic plate should be greater than the "skin depth" of the material to prevent the transmission losses. If the condition is followed then the transmission losses become approximately zero and therefore, can be neglected. In this thesis, the thickness of the basement material is taken much greater than the skin depth of that material under frequency range of interest. Skin depth can be calculated as,

$$\delta = \sqrt{\frac{1}{\pi f \mu \sigma}} \tag{3.15}$$

where f is the frequency, μ is the permeability and σ is the conductivity of the material. Once the transmission losses are neglected, the only threat left to the perfect absorption is the reflection part which can be minimize using the geometric parameter optimization. In order to ensure the perfect absorption, the effective-impedance of the absorber should match with the free-space impedance. Under this position, the reflection and transmission of the incident radiation becomes zero and assures the perfect absorption.

3.3 Analysis Approach

The simulation software used to model and characterize the designed absorber is based on the finite integration technique (FIT). Frequency domain solver of this simulation software is employed to investigate the absorption behavior of the proposed structure. All of the proposed absorber designs are for solar cell applications, therefore, the selection of basement material, morphology, material properties, and the absorption behavior is examined in the solar frequency region that is 100 THz to 1000 THz. Since the solar frequency spectrum is very broad and exhibits distinct properties in each region thus it is divided into infrared, visible and ultraviolet regions for some of the designs and investigation is done separately to get more accurate results. Appropriate boundary conditions are chosen for each design in the simulation. The detailed information about the boundary conditions selected for each model is provided in the related sections. In general, periodic boundary conditions are employed along the x and y-direction whereas along the z-direction open and open add space boundaries are used. Periodic boundary conditions imitate infinite virtual unit cells along the x and $y - directions$ so it also considers the interaction between the designed unit cell with the adjacent

virtual unit cells [68]. In this study, only the unit cell of the photovoltaic absorber is designed therefore, it is more appropriate to use periodic boundary conditions to examine the optical and electrical properties of the unit cell as an entire system [69].

It is assumed throughout this research that the propagation direction of the incident EM radiation is in the z-direction unless stated that the polarization incident waves assumed are transverse electric and magnetic mode (TEM). However, light can propagate in other modes, for instance, transverse electric (TE) and transverse magnetic (TM) modes [70]. In transverse electromagnetic mode (TEM), both electric and magnetic field are always perpendicular to each other and transverse to the direction of the wave travel. In TE mode, an electric field is transverse to the wave propagation direction whereas the magnetic field is along the direction of propagation, known as H-field. In TM mode, a magnetic field is transverse to the wave propagation direction whereas the electric field is along to the direction of propagation, known as E-field. All the modes are analyzed for each design.

Software divides the structure into small elements called mesh and each element is referred to as a mesh cell. The selection of size and type of meshing used for the discretization of the computational model is another important issue while performing electromagnetic simulations which plays a very critical role in the accuracy and speed of the simulations. The accuracy of the results is highly dependent on the type of the mesh and its density. If the specified mesh density is not sufficient to solve the EM simulation, then the obtained results will not be reliable [71]. Throughout this study, hexahedral and tetrahedral mesh types are used with "adaptive mesh refinement". When adaptive mesh refinement is enabled, it increases the number of mesh cells gradually and refined until the s-parameters converges to the defined level of accuracy. The accuracy level of the adoptive mesh refinement is set to be $1x10^{-6}$. Mesh adaptation ensures the adequate mesh density generation for the consistent (valid) and reliable results.

The obtained simulation results are in the form of s-parameters from which we can get the reflection and transmission coefficients. Optical absorption $A(\omega)$ as a function of frequency can be determined by two basic parameters, reflection $R(\omega)$ and transmission $T(\omega)$ as illustrated in equation (3.16). As described earlier, transmission can be neglected because of the metal ground plane thickness more than the skin depth of the material. Thus, equation (3.16) only concentrates on reflection coefficient and reduces to equation (3.17) to calculate the absorption using acquired simulation results that are scattering parameters (S11 and S21) [72]–[74].

$$A(\omega) = 1 - R(\omega) - T(\omega) \quad (3.16)$$

$$A(\omega) = 1 - R(\omega) \quad (2.17)$$

CHAPTER 4

VALIDATION

4.1 Introduction

Validation is the most crucial part of the research to make sure that the obtained simulated results are reliable and accurate. Therefore, this chapter covers the verification of the achieved results by a prior art examination and a preliminary design. For this purpose, two types of validation methods have selected; numerical validation approach and theoretical validation approach. Numerical validation technique includes both verifications through formerly reported nanotube based metamaterial absorber from the literature and validating the simulation software used in the current study by different simulation software. Theoretical validation approach is based on interface theory.

4.2 Numerical Validation

Several computer simulation softwares are available that use different solving methods. From all of them, three most widely used methods for the numerical analysis of the electromagnetics are; Finite Element Method (FEM), Finite Difference Time Domain (FDTD), and Finite Integration Technique (FIT) that has been discussed and utilized for the validation.

FEM uses partial differential form of the Maxwell's equations to comprehending the solutions for the boundary value electromagnetic problems. This solver divides the entire domain into small elements and analyses these subdomains using interpolation function. This method is highly flexible in designing complex curvilinear structures, however, it requires large memory and thus, increase the simulation time.

FDTD also uses partial differential form of the Maxwell's equations to comprehending the solutions for the electromagnetic problems. This solver is independent of iterations which increases the accuracy of the complex designs. However, it requires grid differential form of the entire domain to analyse which unnecessarily increases the computation time. So that this solver is not preferable for the smaller structures.

FIT uses integral form of Maxwell's equations and converts them into linear system of equation to analyse the solutions for the electromagnetic problems. FIT and FDTD, both methods provide almost similar results but it requires less memory and time to solve the

complex structure. It allows parallel computation and provides more accuracy in complex structures simulations.

In this thesis, all simulations are carried out using finite integration technique (FIT) based CST (Computer Simulation Technology) microwave studio software. For the validation of currently proposed metamaterial absorbers, a MTM absorber from the literature designed by Deng et al. has been selected. Deng et al. studied metamaterial absorber based on gold nanowires operating in the frequency range of 120 THz to 250 THz. In their modelling, Deng et al. employed finite element method (FEM) based COMSOL simulation software by adopting electric boundary condition in *x-plane* and magnetic boundary condition in *y-plane*. Their proposed structure is made of two layers; the bottom metallic thick layer composed of gold and gold nanowires embedded in an alumina host. The unit cell of their design is presented in Figure 4-1. The periodic dimension "*x*" of the unit cell is 600 nm and the bottom gold substrate has a thickness *h* = 140 nm. The gold nanowire cavities are of 6 by 6 array with each tube radius *r* = 12.5 nm and center-to-center distance of 60 nm. The nanotube array is inserted in a host that make a cubic shape with *y* = 360 nm and *L* = 140 nm. The optical properties of alumina is described by the permittivity that is taken as $\varepsilon_d = 3.0625$, whereas gold is defined by Drude-model as in Equation (4.1)

$$\varepsilon_m(\omega) = 1 - \frac{\omega_p^2}{\omega(\omega + i\gamma_0)} \tag{4.1}$$

The Drude-model parameters utilized for the gold are; $\omega_p = 1.37 \times 10^{16}$ rad/sec (plasma frequency) and $\gamma_0 = 4.09 \times 10^{13}$ rad/sec (bulk collision frequency). To calculate the absorption of the proposed MTM absorber structure they have used the relation A = 1 – R, since they assumed zero transmission due to have the thickness of the bottom plate more than skin depth of the gold material. Absorption results they have obtained are under normal incident condition, shown as red doted curve in Figure 4-2. Their designed MTM absorber provides single-band with almost 100% absorption at resonant frequency 187 THz. The MTM absorber proposed by Deng et al. presented in Figure 4-1 is redesigned and characterized by using FIT based numerical solver. Similar absorption results with 100% absorption at resonant frequency of 187 THz are achieved by redesigning the model as shown in Figure 4-2 with solid black curve. The simulation results for both method FEM and FIT based solver are in agreement with each other which indicate the verification of the software used throughout this thesis and also the verification from the prior art investigation.

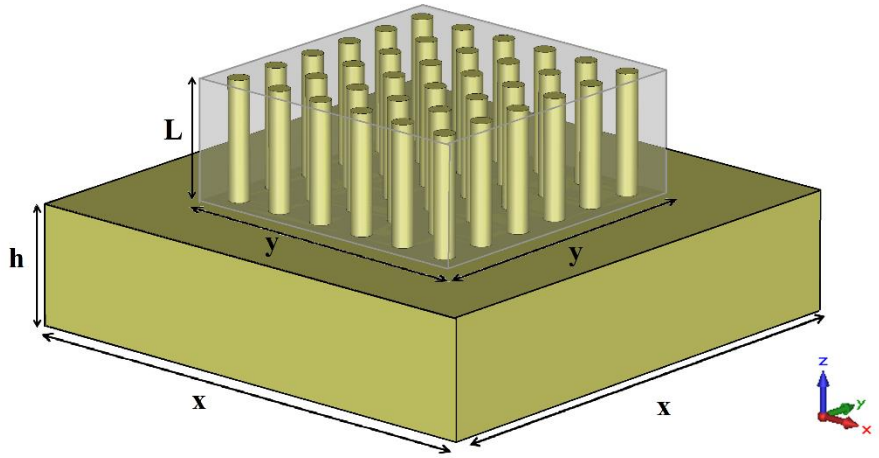

Figure 4-1: The unit-cell and geometric parameters of the proposed MTM absorber designed by Deng et al. using COMSOL (FEM based solver).

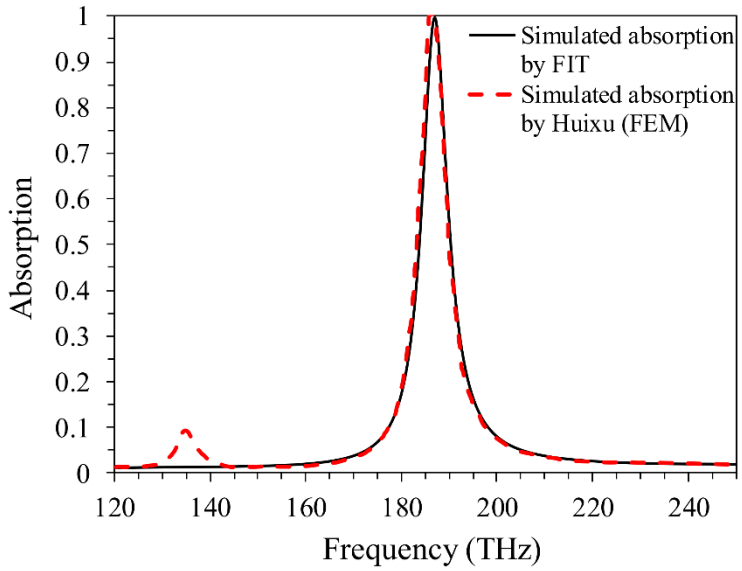

Figure 4-2: Absorption results obtained by Deng et al. using FEM solver (red curve) and absorption results achieved by redesigned and simu+6lated by FIT based solver (black solid curve).

4.3 Theoretical validation

One of the techniques for analysis and theoretical validation of MTM absorber is interface theory, which has been proposed by Cheng in 2012 [75]. Cheng employed multiple-reflections interface-model to demonstrate an insignificant field around two closest metallic films in a regular MTM absorber. According to his approach, if two metallic layers are decoupled then multiple reflections between the dielectric layer and metal will need to

observe. Therefore, combination of analytically solved and numerically simulated results proved that the maximum absorption in a MTM can be an effect of interface or magnificent placement of electromagnetic waves instead of excited magnetic resonances. When first interface theory has been published, several researchers have attracted to this theory [76], [77] but their investigations were restricted to normal incident waves. Afterwards, extended interface theory was introduced by Huang et al. [78] for both oblique and normal incident waves. In this work, interface and extended interface theories are combined to validate the numerically simulated results.

The model selected for the validation is shown in Figure 5-1. Numerical results obtained by the software of this design are verified using the interface theory [75]. Generally, the verification process involves the impedance matching caused by altering permittivity and permeability of the MTM absorber design. Simulated design is comprised of three layers along with basement metallic layer. The thickness of the ground metal layer much greater than the skin depth is applied to block the transmission. Moreover, the EM waves from the metal layer reflect back to the dielectric layer to achieve the maximum absorption, this process is named as "coupled model". The extended interface theory, which is applied for theoretical verification of the MTM absorber for both normal and oblique incident wave, requires the removal of bottom metallic plate is named as "decoupled model". Coupled and decoupled models are presented in Figure 4-3 (a) and (b). Numerically simulated scattering parameters are utilized in superposition and interface equations to calculate the absorption coefficient.

Three possibilities can occur as incident radiations strikes to the surface. Incident waves can reflect back to the atmosphere from the region-1 as shown in Figure 4-3. Incident waves that are not reflected back can transmit from region-1 to region-2 and the rest will be absorbed. In this theory, it is assumed that the layer 1 has almost zero thickness. The coefficients of scattering parameters are defined as; $S_{11} = |S_{11}|e^{j\theta_{11}}$ which denotes the reflection coefficient from region-1 to region-1, $S_{12} = |S_{12}|e^{j\theta_{12}}$ is the transmission coefficient from region-1 to region-2, $S_{21} = |S_{21}|e^{j\theta_{21}}$ is the transmission coefficient from region-2 to region-1, and $S_{22} = |S_{22}|e^{j\theta_{22}}$ is the reflection coefficient from region-2 to region-2. The extended interface model which calculates the total reflected EM radiations from the region-1 to region-1 can be calculated by Equation (4.2).

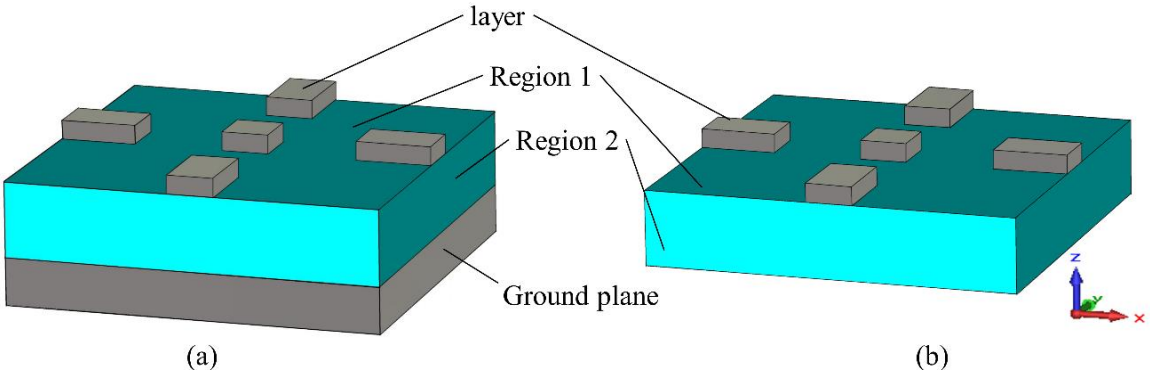

Figure 4-3: Unit-cell of the MTM absorber design (a) Coupled model (b) Decoupled model

$$\sum S_{11} = S_{11} + S_{12}e^{-j(2\beta+\pi)}S_{21} + S_{12}e^{-j(2\beta+\pi)}\left(S_{22}e^{-j(2\beta+\pi)}\right)S_{21}$$
$$+ S_{12}e^{-j(2\beta+\pi)}\left(S_{22}e^{-j(2\beta+\pi)}\right)^2 S_{21} + \ldots + S_{12}e^{-j(2\beta+\pi)}\left(S_{22}e^{-j(2\beta+\pi)}\right)^n S_{21} \quad (4.2)$$

where, $\beta = kd$ is the complex propagation phase, k is the wavenumber for region-2, and d is the propagating displacement of the transmission waves between layer-1 and ground plane. Simplification of Equation (4.2) provides Equation (4.3), which is rearranged by superposition principle to obtained total reflection region-1 to region-1 by Equation (4.4).

$$\sum S_{11} = S_{11} + S_{12}e^{-j(2\beta+\pi)}S_{21}\left(\sum_{n=0}^{\infty}(S_{22}e^{-j(2\beta+\pi)})^n\right) \quad (4.3)$$

$$\sum S_{11} = S_{11} + \frac{S_{12}e^{-j(2\beta+\pi)}S_{21}}{1 - S_{22}e^{-j(2\beta+\pi)}} \quad (4.4)$$

By introducing the S-parameters and their phases values demonstrated in Figure 4-5 (a) and (b), total reflection region-1 to region-1 can be calculated by Equation (4.5).

$$\sum S_{11} = |S_{11}|e^{j\theta_{11}} + \frac{|S_{12}||S_{21}|e^{-j(2\beta+\pi-\theta_{12}-\theta_{21})}}{1 - |S_{22}|e^{-j(2\beta+\pi-\theta_{22})}} \quad (4.5)$$

In MTM absorber design, obtained results of magnitude of S_{12} and S_{21} are same and the Equation (4.5) can be simplified to use in the theoretical investigation.

$$\sum S_{11} = |S_{11}|e^{j\theta_{11}} + \frac{|S_{12}|e^{-j(2\beta+\pi-2\theta_{12})}}{1 - |S_{22}|e^{-j(2\beta+\pi-\theta_{22})}} \quad (4.6)$$

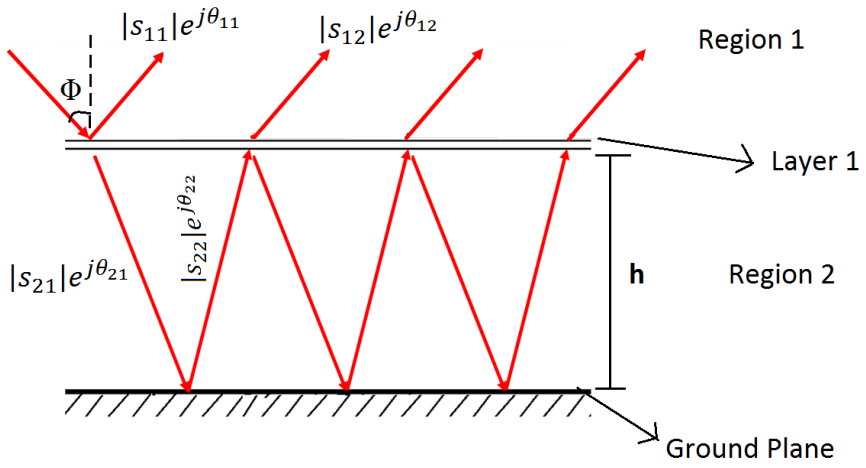

Figure 4-4: Multiple reflection and illustration of the rays and their coefficients of interface theory model

Interface theory mentioned above is applied to validate the simulated wide-band MTM absorber structure presented in Figure 4-3. Ground metallic place is detached before performing the simulation, decoupled system is shown in Figure 4-3(b). The numerically simulated S-parameters both phase and magnitude are given in Figure 4.5 (a) and (b), which are utilized to calculate total s-parameters from Equation (4.6) and the results are compared in Figure 4-6. Theoretically calculated (decoupled) and simulated (coupled) results have the same magnitude of absorption at all resonance frequencies which verified the results.

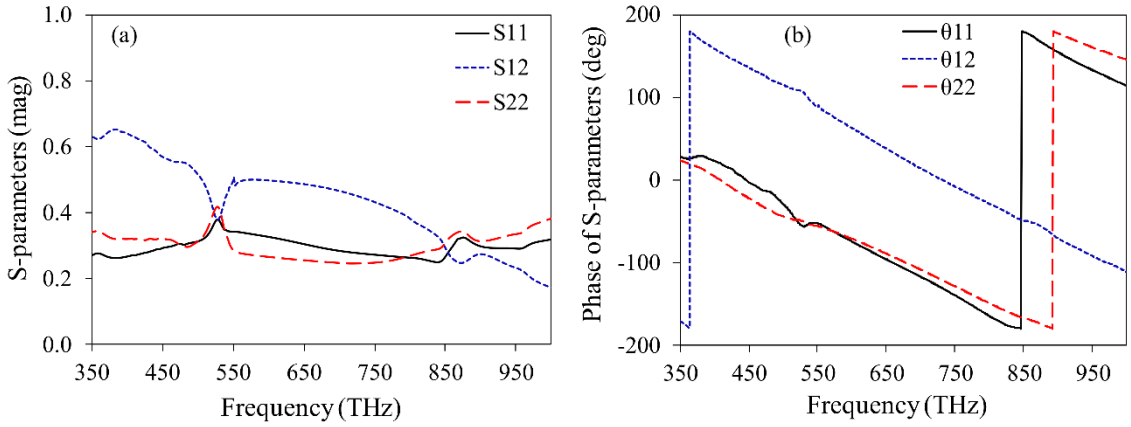

Figure 4-5: (a) Magnitude of S-parameters obtained from the simulated decoupled model, (b) Phase of S-parameters obtained from the simulated decoupled model.

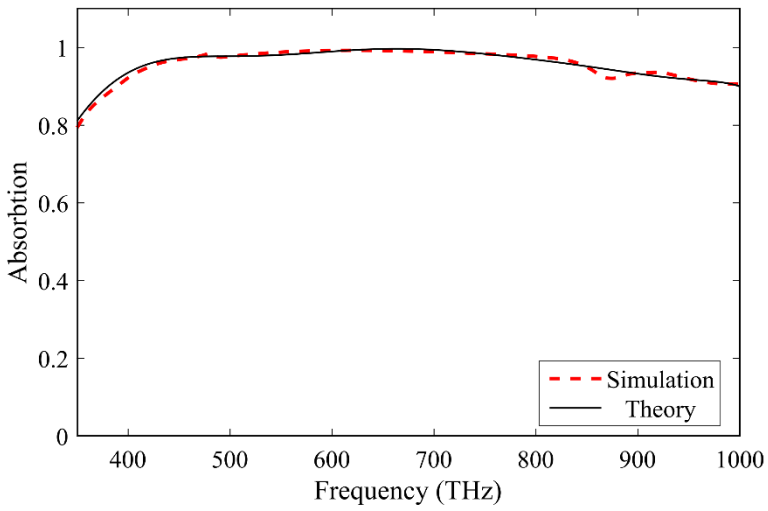

Figure 4-6: Absorption results of the coupled (FIT based solver) and decoupled (interface theory) model.

4.4 Conclusions

Theoretical analysis and numerical validation techniques are discussed in this chapter. Software validation is carried out using both prior art investigation and the different solver such as FEM and FIT. Results of interface theory model and simulation are compared which provide the reliable and accurate results.

CHAPTER 5

THIN FILM (6,5) SEMICONDUCTING SWNT METAMATERIAL ABSORBER FOR SOLAR CELL

5.1 Introduction

Carbon nanotube (CNT) is one of the most promising materials to improve the efficiency of solar cells [79]. It possesses exceptional high mobility (10^5 cm^2/Vs) [79], two to three times higher current conversion density than the commonly used metal conductors and has the greater conductivity [80] than the other semiconducting materials. SWNTs are direct bandgap semiconductors [85] and highly absorptive materials with absorption cross-section of 10^{-18} cm^2 per carbon atom [17]. Their manufacturing cost significantly reduces due to simple solution processability [82], scalable fabrication [18], and purification which has been a drawback in conventional solar cell design [12]. Fabrication demand is escalating for the devices capable of manipulating the incident electromagnetic wave through the structure. Advancement in nanostructure fabrication techniques allows for the realization of artificial materials with alluring properties such as negative refractive index, that do not exist in nature, only in metamaterials [83].

Previously reported carbon nanotube metamaterials have mainly focused on one and smaller frequency region. For instance, Hong et al. [83] fabricated SWNT film metamaterial structure, operating in the frequency range of 0.5 to 2.5 THz. In their structure, SWNT film is used as a very thin metallic layer working as a resonator with the silicon dielectric material. Nikolaenko et al. [21] demonstrated a hybrid structure of semiconducting SWNT with photonic metamaterial which was designed to operate in the near-infrared region. Nikolaenko et al. [84] designed a nanostructure plasmonic gold metamaterial with semiconducting SWNT. The structure was proposed for 150 to 200 THz. They also used multiple layers of different materials to enhance the rate of absorption in their structure [84]. Rossella et al. [85] experimentally designed cobalt-filled carbon nanotube magnetic metamaterial for the magneto-electronic devices. In this study, the electromagnetic response of the (6,5) semiconducting SWNT as an active thin film dielectric layer with top aluminum resonator and the bottom thick aluminum ground metallic plate is numerically simulated and analyzed. The flexibility of the proposed design is investigated by changing the geometric parameters of the structure to check the absorption variation. It is found out that the pattern of the

resonances observed in the reflection changes with changing geometric parameters. The proposed design is also simulated for other chiralities including (5,4), (6,4), (7,5), (9,4), and (10,3) and results are compared with (6,5) SWNT to show that the proposed design works best for (6,5) SWNT but also good for other chiral carbon nanotubes in the visible and ultraviolet frequency regions. The proposed metamaterial absorber enhances the absorption capability of the solar cell.

5.2 Design and Analysis

The unit cell of SWNT-metamaterial absorber proposed in this study composed of three layers; aluminum resonator at the top of the dielectric, aluminum metallic bottom ground plate and (6,5) SWNT as a dielectric layer in between metallic layers as illustrated in Figure 5-1. Dielectric layer with a thickness of "*d*" is coupled with the metallic top resonators (with a thickness of "*t*") and bottom plate to enhance the resonance frequencies. The thickness of the ground metal plate "*h*" is selected much larger than the skin depth of the aluminum to stop transmission losses in the studied frequency range. Aluminum and SWNT, are found abundantly [81], inexpensive and pose no harm to the environment [12]. Aluminum is selected based on its low cost, resistance to high temperature, low skin depth as compared to gold and silver, and its ability to reflect in the high-frequency radiations [86]. The frequency dependent material properties (dielectric constant) of the aluminum is taken from the Palik's studies [87]. The parametric and dimensional characteristics of the proposed unit cell design are given in Figure 5-1. The arrangement, orientation and dimensions of the resonators in the proposed structure bring uniqueness and facilitate maximum absorption. The lateral dimension of the proposed absorber structure must be less than the wavelength of the incident radiations, therefore the thickness of the total absorber design is preferred to be less than the $(h + d + t)$ wavelength [88]. The resonator geometric configuration consists of a central patch and the four identical strips. This arrangement of resonator is responsible for the generation of the wide-band absorption in the frequency range of interest.

The electromagnetic response of the proposed design is computationally analyzed using full-wave electromagnetic solver established on finite integration techniques to solve Maxwell's equations. Several simulations are performed to fully understand the absorption mechanism by varying the design parameters. Optimal parameters are achieved by changing and simulating all parameters together provided in Table 5-1. The polarization of incident electromagnetic radiations is chosen such that the electric (E) and magnetic (H) fields propagate parallel to the geometric plan that is E-field along x-direction and H-field along the

y-direction. Whereas the wave vector (k) is perpendicular to the structure plan [89]. Throughout the numerical simulations, the boundary conditions were periodic in x and y-plane and open add-space in the z-plane. All simulations are executed under normal incidence with transverse electromagnetic (TEM) wave unless the other modes of propagation are indicated. Other propagation modes can be transverse electric (TE-mode) and transverse magnetic (TM-mode). The proposed design operates in the visible and ultraviolet frequency region (350 to 1000 THz).

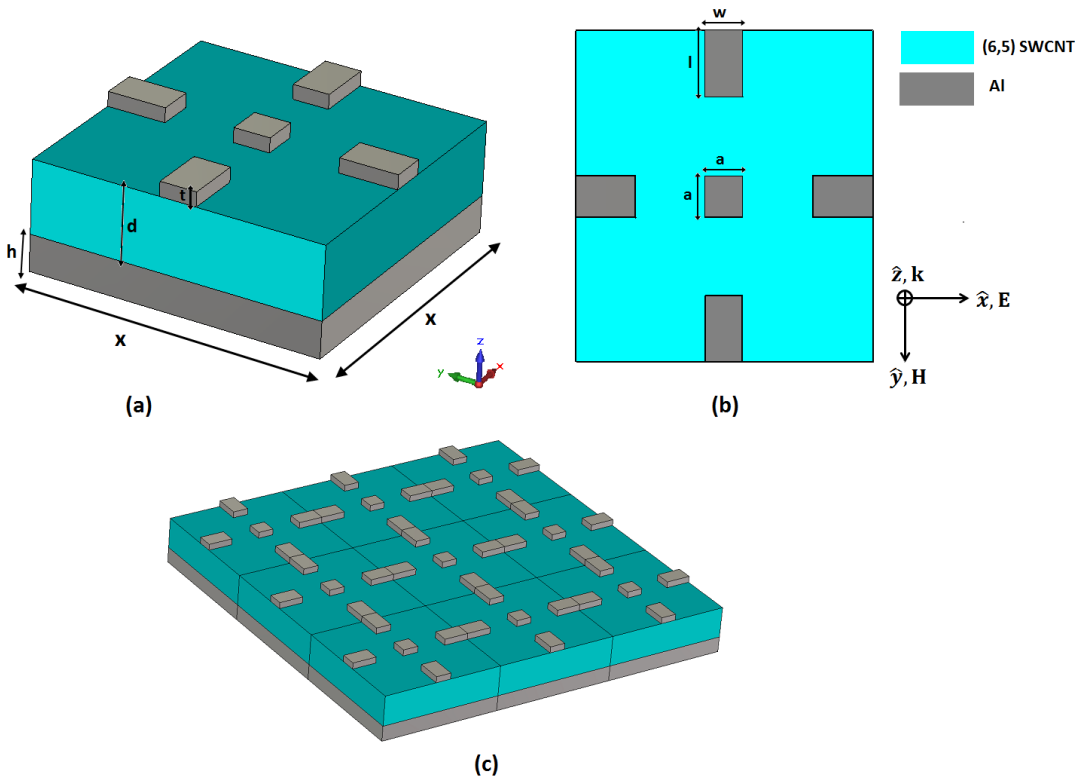

Figure 5-1: (a) Isometric view of unit-cell and geometric parameters of the (6,5) SWNT metamaterial absorber. (b) Top view of the design. (c) Complete proposed absorber design.

Table 5-1: Geometrical dimensions of the proposed absorber design.

Parameter	*a*	*d*	*h*	*l*	*t*	*w*	*x*
Value (nm)	50	100	50	80	20	50	400

The optical absorption $A(\omega)$ strongly depends on its reflection $R(\omega)$ and transmission $T(\omega)$ parameters, and can be estimated as; $A(\omega) = 1 - R(\omega) - T(\omega)$. Therefore the bottom metallic plate is designed thick enough (more than its skin depth) so that it performs like a mirror and completely blocks transmission ($T(\omega) = 0$) [90]. Ambiguity related to the

reflection coefficient has much more effect on the results as compared to the change of transmission coefficient. A minor discrepancy in the reflection coefficient leads to major transformation on the material's parameters while the impact of transmission coefficient is not sensitive [15]. Through a careful modification of the geometrical parameters and the appropriate material selection, the SWNT-metamaterial design parameters are engineered to match the free-space parameters at the wide-band resonance frequency. Thus, the free-space impedance ($Z_0 = \sqrt{\mu_0/\varepsilon_0} = 377\Omega$) is matched with the impedance of the proposed absorber design ($Z(\omega) = \sqrt{\mu(\omega)/\varepsilon(\omega)}$) structure. The parameters μ_0 and ε_0 are the free-space magnetic permeability and electric permittivity while $\mu(\omega)$ and $\varepsilon(\omega)$ are the magnetic permeability and electric permittivity of the metamaterial absorber. This process results in achieving the minimum (negligible) reflection coefficient which leads to the higher absorption (almost unit absorption rate) in the broad frequency range.

5.3 Result and Discussion

Simulated absorption and reflection of the unit cell absorber design in the visible and ultraviolet frequency region are shown in Figure 5-2. A wide-band absorption is obtained as a result of the combination of resonant frequencies which are combined together to form a wide-band with maximum absorption near unity. Spectral matching of the active material (SWNT) with the metamaterial resonance causes higher absorption [84]. Since the absorption rate is more than 90% throughout 450 to 1000 THz frequency range, four different frequencies 450 THz, 500 THz, 627 THz, and 750 THz are selected at which absorption rate are 97.4%, 98.3%, 99.2% and 98.4%, respectively, to completely realize the function of the resonators.

Wide-band absorption is the outcome of the electromagnetic response generated by the strong coupling of each strip resonator and the patch with the dielectric and the ground plane. To investigate the mechanism of the wide-band absorption, separate numerical simulations for one, two, three and four strip resonator with the center patch are carried out. The absorption behavior of single, double, triple, and quadruple strips with the center patch are given in Figure 5-3. From Figure 5-3, it can be clearly observed that when single resonator with the center patch is used, the absorption rate between 350 to 600, and 850 to 1000 THz is considerably low when compared to the quadruple strip resonator. When the number of strips are increased to double and triple, absorption rates also increase, and in the case of quadruple strips, maximum wide-band nearly unity (99.2%) absorption at 627 THz is achieved. Central square patch appears not to be providing any individual peak but it helps the strips to enhance the magnitude of the resonance generation by the strips.

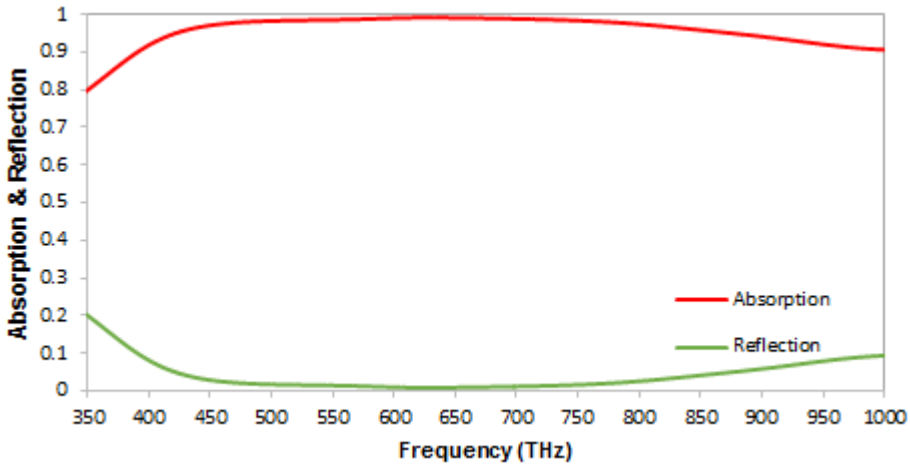

Figure 5-2: Absorption and reflection curves of the wide-band absorber design in the visible and ultraviolet frequency region.

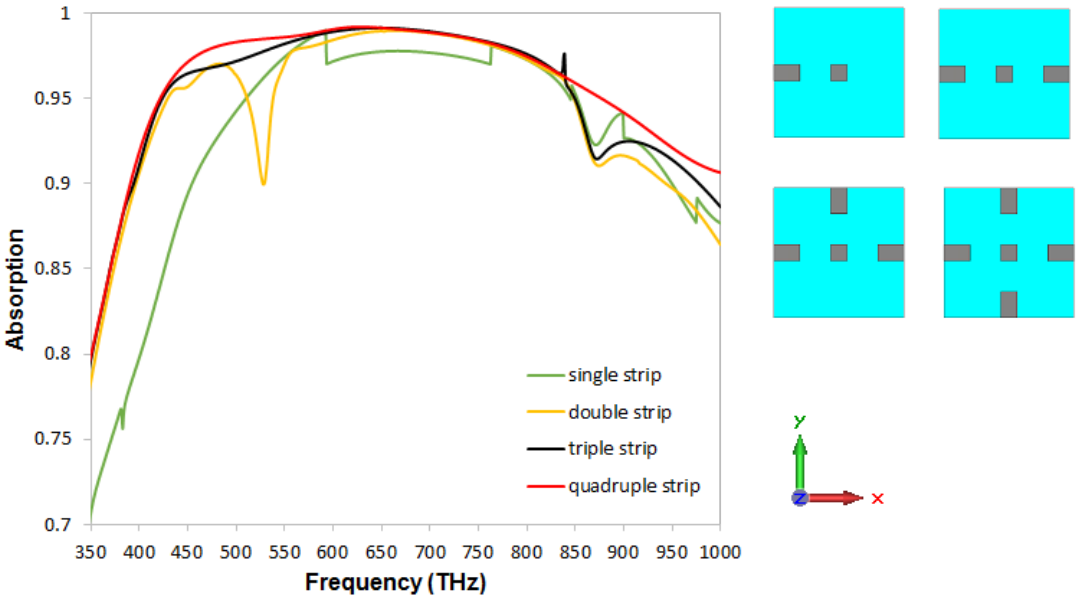

Figure 5-3: Simulated absorption behavior of the single, double, triple and quadruple strips with the center patch.

In addition to the (6,5) SWNT as dielectric layer, the absorption behavior of the other chiral SWNTs such as (5, 4), (6, 4), (7, 5), (9, 4), and (10, 3) are also investigated in the same frequency region 350 to 1000 THz for the proposed metamaterial absorber design. Simulated results for these chiral SWNTs as dielectric layer are presented in Figure 5-4. For the (5,4) SWNT, three peaks are established at 528 THz, 756 THz and 821 THz with 94.27%, 67.17%, and 99.79% absorption, respectively. Fluctuating absorption behavior of the (6,4) SWNT is observed with two broad peaks at 580 THz and 821 THz with absorption rate 97.4% and

99.45%, respectively. Impedance mismatch between resonator and bottom layers causes multiple reflections which impede the major pulses, and reveals the variation pattern [58].

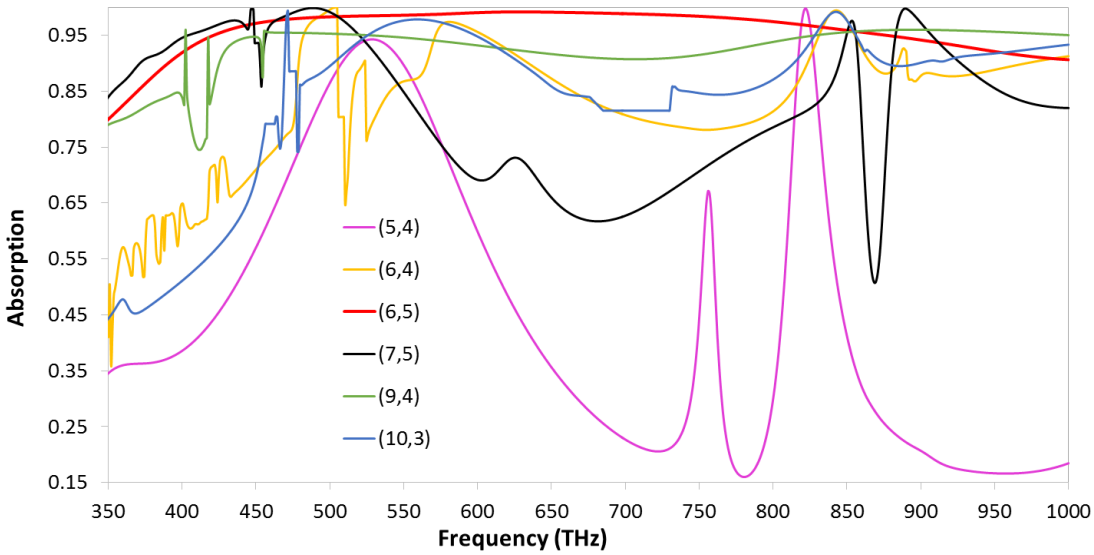

Figure 5-4: Comparison of the absorption spectra of the different chiral SWNT in the visible and ultraviolet frequency region

For the (7,5) SWNT dielectric layer, one board peak at 488 THz with 99.8% absorption while two narrow peaks at 853 THz and 889 THz with 97.6% and 99.79% absorption rates are achieved, respectively. Single wide-band with 95% maximum absorption is realized for the (9, 4) SWNT throughout the entire region, whereas (10, 3) SWNT has two broad peaks at 559 THz and 842.5 THz with 97.8% and 99.1% absorption rates, respectively. It has been experimentally [4] evident in the literature that the larger diameter of CNTs exhibit inhomogeneous and highly dispersed films which reduce the transparency and conductivity so that CNTs should be selected with a smaller diameter to increase the rate of absorption and to produce the high-quality film [4]. It can be concluded that the suggested design is a good candidate for all chiral SWNTs investigated but best absorption is achieved with (6,5) SWNT. However, this metamaterial design can further be improved by some modifications in the geometric dimension for the other chiralities as it is done for the (6,5) SWNT.

5.3.1 Parametric study

Metamaterial structural properties are highly dependent on the permittivity and permeability, which are inevitably affected by the geometry of the metamaterial. Therefore, p parametric analysis is done to realize the influence of geometry on the absorption response and the results are provided in Figure 5-5. Note that best chosen results are shown with red color in all the

plots. Firstly, the effect of the dielectric thickness "*d*" on the absorption is investigated by keeping other parameters fixed which are shown in Figure 4-5(a). Dielectric thickness increased and decreased from 100 nm with intervals of 10 nm. The absorption peak diminished from 350 to 800 THz at $d < 100$nm while at $d > 100$nm declines from 600 to 1000 THz. The absorber design is oversensitive to the dielectric thickness where wide-band near unity absorption is achieved at $d = 100$ nm. The wide-band unity absorption accomplished by the impedance matching at resonance frequencies where the electric resonance between the top resonator and bottom metallic plate are coupled to generate a magnetic response. This condition ensures that the electric permittivity and magnetic permeability of the absorber match with the free space, thus, minimizing reflection.

Secondly, as discussed in earlier sections, resonators at the top of the dielectric play a very significant role in the absorption rate at resonance frequencies, which is confirmed by varying the "*l*" length of the strips resonators reported in Figure 4-5(b). The length of the strips changed around $l = 80$ nm by increasing 20 nm. Absorption rate remained higher than 95% for all the strip lengths from 600 THz to 800 THz, however, one can easily notice that as the length of the strip is increasing, the bandwidth is narrowing down, resulting in lower absorption from 350 to 600 THz and 800 to 1000 THz frequency ranges. Maximum absorption reached at a smaller value at $l = 80$nm. This situation is mainly caused by the interaction between resonators, whereby adjusting the length of the strips, the wide-band absorption can be assured with absorption enhancement. In addition to the length of the strips, the thickness of the resonator also determines the absorption strength presented in Figure 4-5(c). It is obvious from Figure 4-5(c) when the thin resonator is employed narrow peak is achieved from 550 to 750 THz. However, as the thickness increased, the bandwidth of the absorber becomes broader with a slight drop in the absorption magnitude. The reason is when the "*t*" was set to be smaller 5 nm, it was not enough to create peak absorption response. Maximum absorption was attained at $t = 20$ nm, whereas if the thickness continued to increase, the absorption spectra again start to decrease because the metallic parts of the structure turn to act like an optical mirror. Thus, 20 nm thickness is chosen for the higher absorption which has perfect coordination concerning reflected and transmitted waves. Effect of the variation in strips width on the absorption is also analyzed, as presented in Figure 4-5(d). As it can be understood from the Figure, all of the curves have slight decrement in the center of the broad spectra when the width of the strip "*w*" is increasing, however it has positive effect on the absorption at the two corners of the broad spectrum up to $w = 50$ nm, after which absorption rate starts to decrease.

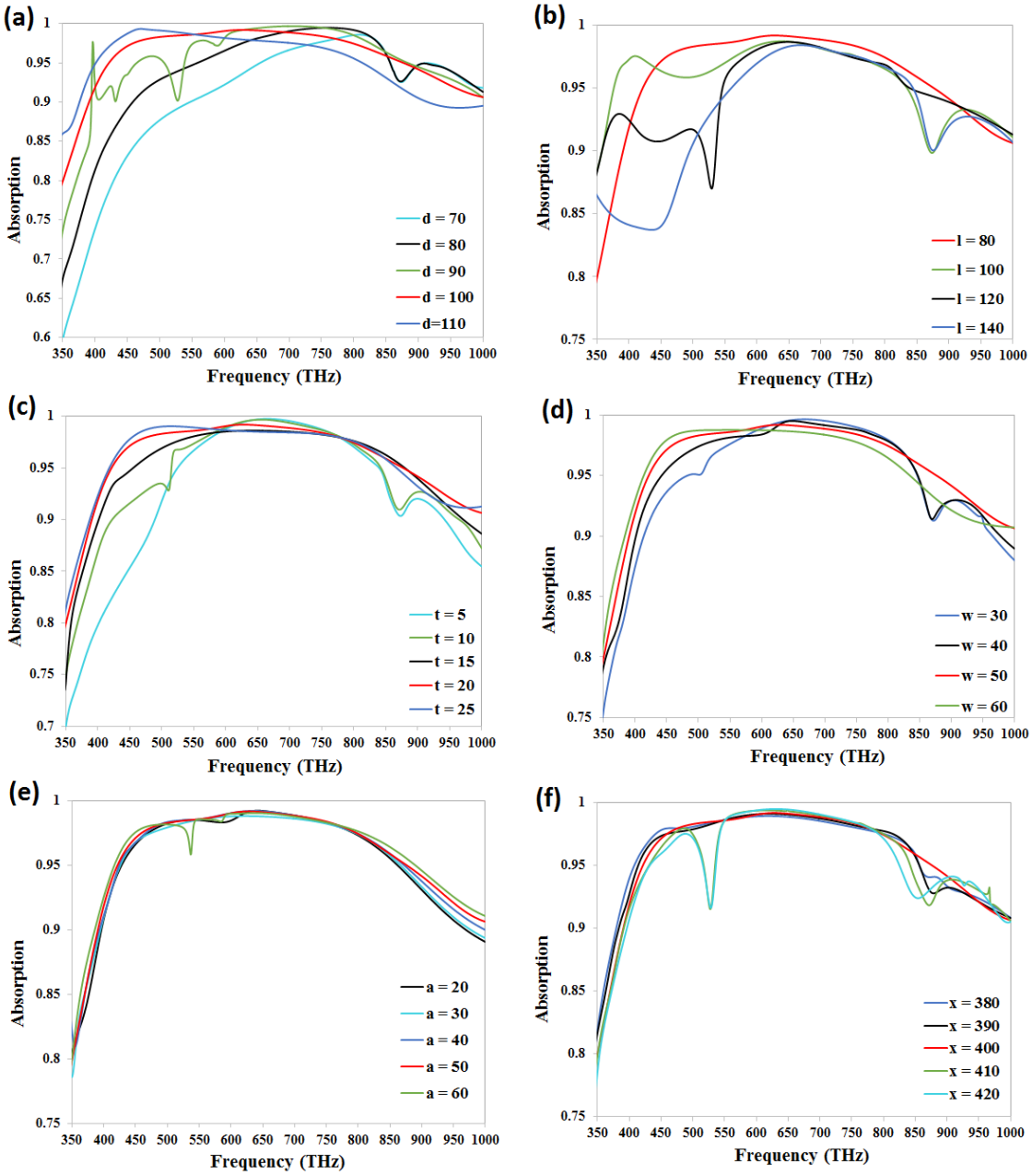

Figure 5-5: Simulated absorption results for (a) dielectric thickness '*d*', (b) length of the strips '*l*', (c) thickness of the resonators '*t*', (d) width of the of the strips '*w*', (e) patch dimension '*a*', and (f) absorber periodicity '*x*'.

Lastly, the study on the effect of the central patch and the unit cell periodicity is performed and simulated results are given in Figure 4-5(e) and (f). Central square patch is between 20 to 60 nm with a period of 10 nm. As mentioned in the previous paragraph, the central patch is not providing any individual peak but it helps the strips enhance the magnitude of the resonance generating by the strips. Therefore, the Figure exhibits that very slight improvement is observed with increasing the patch size up to a = 50nm after which it declines.

The unit cell periodicity also does not contribute too much to the absorption. Simulation is done both increasing and decreasing the unit cell periods from 400 nm with a step width of 10 nm. When the length of the period was less than 400 nm, absorption was almost the same with slight drops. However, in the case of more than 400 nm periodicity, abrupt decline appears at 500 nm and 850 nm, so that 400 nm length of the periodic cell is selected for all the simulations.

5.3.2 Fields and current distributions

In order to get insight of the physics behind the absorption, results of electric and magnetic fields and the current distributions at four resonant frequencies 450 THz, 500 THz, 627 THz, and 750 THz are illustrated in Figure 5-6, Figure 5-7, and Figure 5-8, respectively. As it can be observed, results for the resonance frequencies at 450 THz and 500 THz display almost the same type of electric and magnetic fields distributions. For these two resonances, absorption response is generated by all resonators. The strong electric field is localized around the inner edges of the two horizontal strips facing towards the patch, two sides of the vertical strips and the both sides of the patch, whereas the magnetic field at these resonances is originated by only two horizontal strips. The intense E-fields concentrated around the resonators instigate chare on the surface which generate circulating current. The circulating current appears by the coupling between strips resonator and the bottom aluminum plate. Resonance frequency at 627 THz also results because of the electric fields around all strips, however at this frequency, the concentration of the electric field is relatively lower at horizontal strips and the patch, whereas the magnetic field is very strong at the outer side of the horizontal strips. Surface current distribution at this resonance is generated not only by the circulating current at the strips but also by the antiparallel current at the SWNT layer at the position where the circulating current at the strip is focused along the strong parallel current at the SWNT layer caused by the interaction between the bottom aluminum layer and the SWNT layer. Lastly, the resonance frequency at 750 THz is mainly contributed by the structure itself as at this frequency the absorption spectra were already high without resonators. On the other hand, the presence of resonators enhanced the magnitude of the absorption spectra. From the electric field, it can be observed that only vertical strips have smaller contribution at this frequency while there is no electric field at horizontal strips and the central patch. Similarly, magnetic field is only produced by the smaller contribution of the horizontal strips. Surface current also depicts that parallel current is moving through the dielectric layer, however, minimal amount of circulating current is observed at the resonator strips. The resulted E and H fields and current distributions imply that the impedance of the

proposed design corresponded with impedance of free-space leading to the maximum absorption of all the EM waves at the wide-band frequency region.

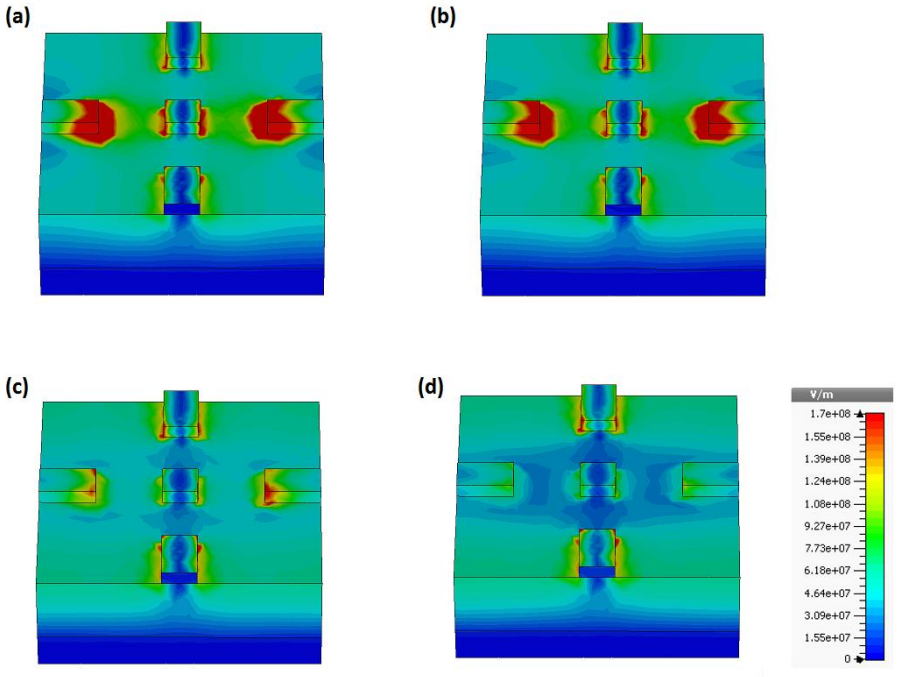

Figure 5-6: Electric field distribution of the proposed absorber design at (a) 450 THz (b) 500 THz (c) 627 THz (d) 750 THz.

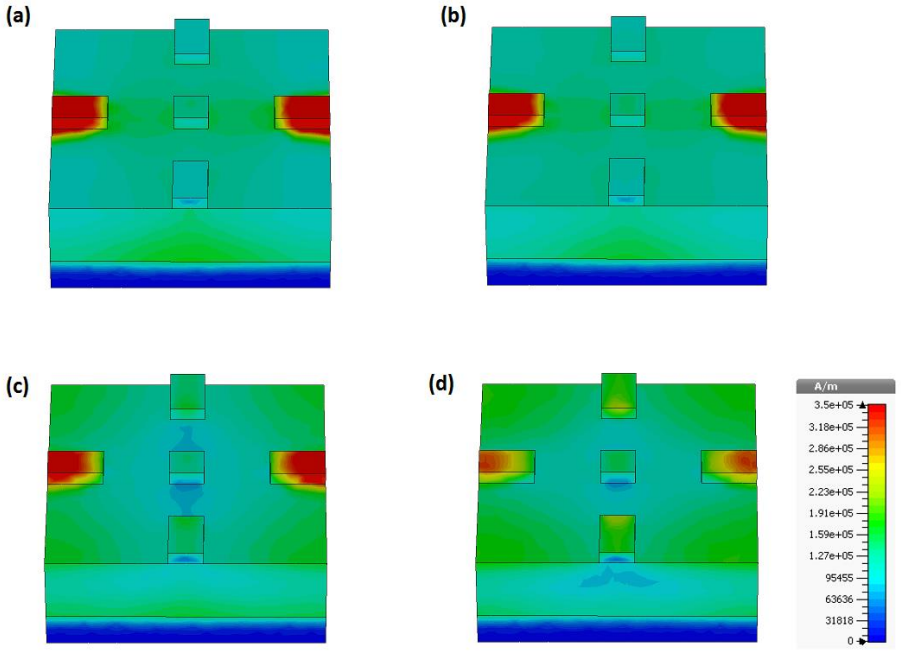

Figure 5-7: Magnetic field distribution of the proposed absorber design at (a) 450 THz (b) 500 THz (c) 627 THz (d) 750 THz.

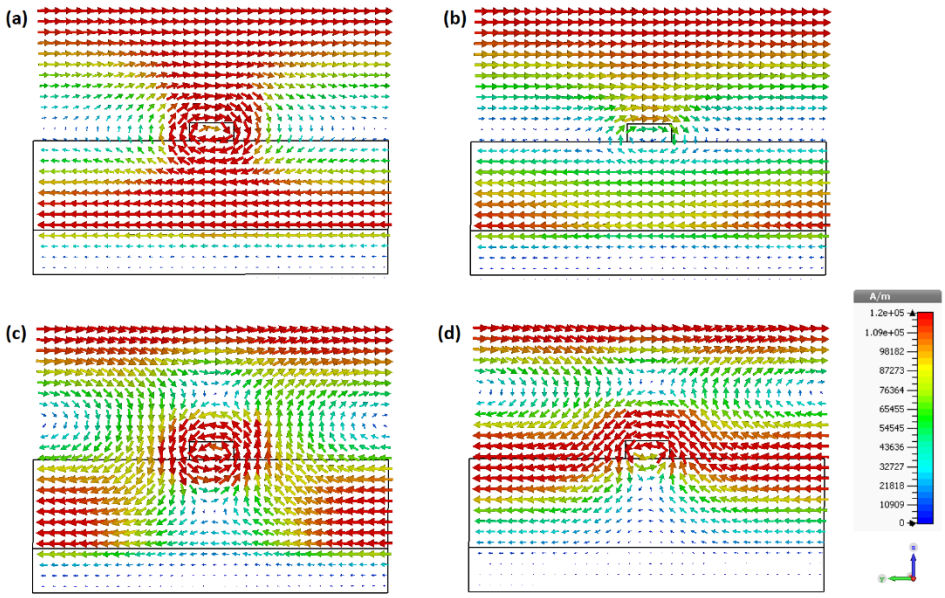

Figure 5-8: Surface current distribution of the proposed absorber design at (a) 450 THz (b) 500 THz (c) 627 THz (d) 750 THz

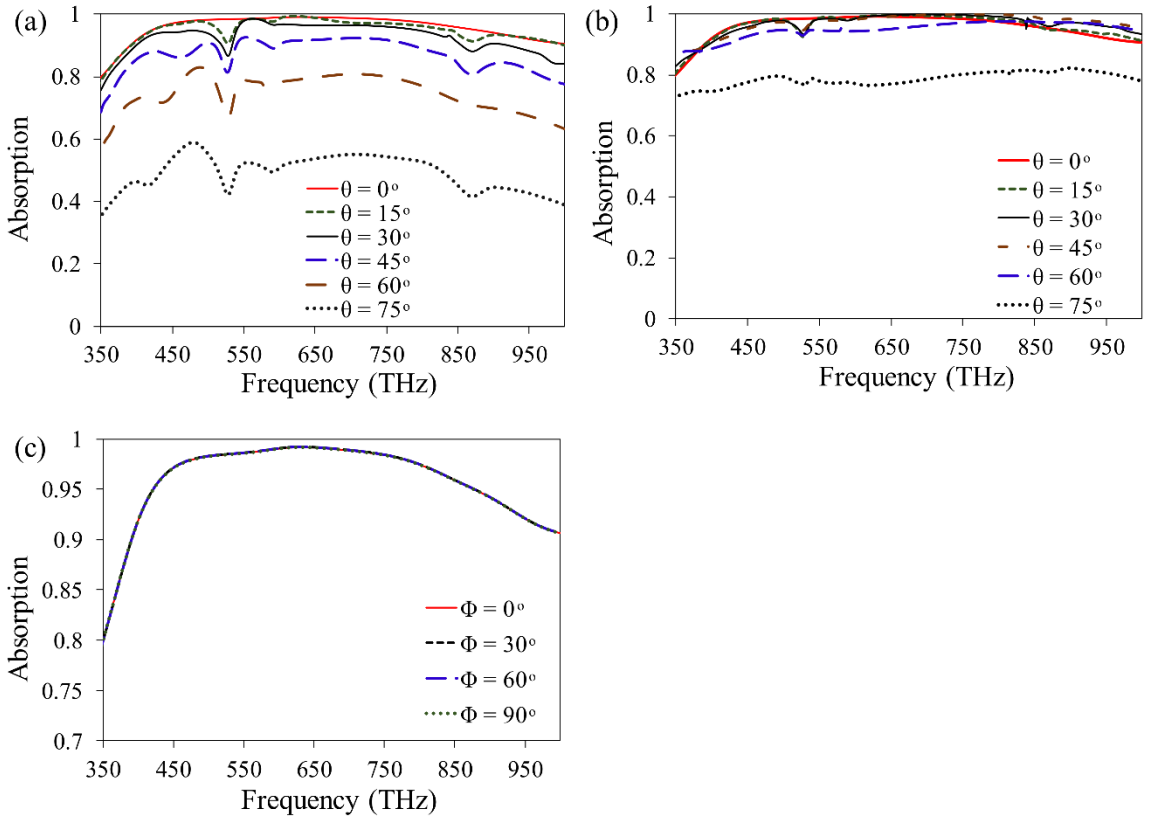

Figure 5-9: (a) Simulated absorption spectra for different incident angles for TE-mode. (b) Simulated absorption spectra for different incident angles TM-mode. (c) Simulated absorption spectra for different polarization angles at normal incidence (TEM mode).

5.4 Polarization and incident angle

In order to further investigate the absorption behavior of the proposed design concerning the radiation sources, simulations under various incidence angles for TE-mode and TM-mode, and for different polarization angles (TEM-mode) are performed. Simulated results of absorption spectra for TE-mode are illustrated in Figure 5-9(a) while Figure 5-9(b) shows the variation in absorption spectra for TM-mode. From the results it can be observed that the effects of the TE-mode are highly sensitive to the incidence angle than those of the TM-mode, particularly at larger angles of 60^{o} and 75^{o}, where minimum rates of absorption are observed. This is due to the dependency of the strength of magnetic field component of the incidence wave on the angle of incidence "θ", which becomes smaller when θ increases [91]. Therefore, for the proposed design at larger incident angles (60^{o} and 75^{o}) the magnetic polaritons are inefficiently excited which reduces the amount of absorption by impedance mismatch and the increased reflection of incident waves. Although, except 60^{o} and 75^{o}, more than 90% absorption rate is achieved. In addition, as shown in Figure 5-9(c) the proposed metamaterial absorber is independent of polarization angles from 0^{o} to 90^{o}. The realization of this behavior is due to the high symmetric characteristics of the proposed structure under study which provides polarization independency under normal incidence (TEM-mode). Thus, it can be stated that the proposed metamaterial absorber is a good candidate for the devices operating in the visible and ultraviolet frequency region especially for the solar cells, where absorbance can be kept high with respect to the polarization angle under normal incidence (TEM-mode).

5.5 Conclusions

A novel wide-band (6,5) SWNT metamaterial absorber structure with near unity absorption in the visible and ultraviolet frequency ranges is numerically simulated and analyzed. The proposed design offers wide-band with a maximum of 99.2% absorption rate caused by strong electric and magnetic fields between the strip resonator and the bottom metallic plate. The proposed design is also compared with the different chiral SWNTs and results are reported. Parametric study of the proposed design is analyzed to provide the insight of absorption mechanism and to realize the effect of geometric parameters on the absorption behavior. The absorber design under investigation possesses high flexibility and is capable of keeping the wide-band with higher absorption. Moreover, an electric and magnetic field with surface current distribution is discussed in details to get the insight of the physics behind the absorption mechanism. Finally, absorption simulations are performed under the different incident and polarization angles and results are found to be polarization independent.

Therefore, the proposed semiconducting (6,5) single-walled carbon nanotube metamaterial absorber turn out to be an outstanding candidate for the maximum absorption in the visible and ultraviolet frequency regions for the solar cell application.

CHAPTER 6

POLARIZATION INDEPENDENT TRIPLE-BAND (5,4) SEMICONDUCTING SWNT METAMATERIAL ABSORBER

6.1 Introduction

Research to control the dielectric constants of the substrate instead of metal film have been demonstrated in the terahertz (THz) region by light illumination [92], heating [93], and electrical bias [94]. More flexibility will be allowed, if optoelectronic properties of the conducting film can be modified by controlling the structure. Though, metal films are not capable of providing the freedom to change the dielectric constant due to having higher carrier density and limitations to alter the optical constants [95]. On the other hand, semiconducting single walled carbon nanotube (SWNT) films can be the best suitable alternative for the metal films in THz region. Solution based treatments of SWNT allow fabrication of optically thick-film without demanding expensive vacuum and provide controllable carrier density by post processing, which assists the alteration of dielectric constant [96], [97].

This paper presents a novel triple-band polarization insensitive metamaterial absorber design and its enhancement with semiconducting single walled carbon nanotube as the dielectric layer for the solar cell application. The EM response of the proposed design is numerically simulated in the visible and ultraviolet region. Flexibility of the design is also analyzed to realize the absorption behavior by controlling the geometrical parameters. Highly flexible MTM absorber design is achieved which is capable of absorbing maximum solar radiations even at larger incident angles while being polarization insensitive.

6.2 Material and Design

Absorption rate $A(\omega)$ of the solar cell is strongly based on two parameters; frequency dependent reflection $R(\omega)$ and the transmission $T(\omega)$ that can be calculated as: $A(\omega) = 1 - R(\omega) - T(\omega)$ [98]–[100]. However, rate of reflection and transmission depend on scattering-parameters [$R(\omega) = |S_{11}|^2$ and $T(\omega) = |S_{21}|^2$] which can be described by the following equations [101].

$$S_{11} = \frac{\sqrt{Power\ reflected}}{\sqrt{Power\ incident}} \tag{6.1}$$

$$S_{21} = \frac{\sqrt{Power\ transmitted}}{\sqrt{Power\ incident}} \tag{6.2}$$

In order to maximize the absorption of the solar cell, $R(\omega)$ and $T(\omega)$ should be minimized to a value of nearly zero. One of the main approaches adopted to achieve this goal is the use of metal-semiconductor layer in periodic arrangement along with the top resonator. Therefore, using geometrical optimization process, the MTM absorber impedance ($Z(\omega)$) can be matched with the free space impedance (Z_0 = 377Ω) at the resonance frequency which results in remarkable reduction in reflection by the MTM structure. Besides, reflection of the MTM absorber can also be minimized (to nearly zero) by achieving minimum values of effective electric permittivity ($\varepsilon(\omega)$) and magnetic permeability ($\mu(\omega)$). Consequently, for having perfect absorption, $\varepsilon(\omega)$ and $\mu(\omega)$ can be adjusted to absorb both electric and magnetic fields [102]–[104]. On the other hand, transmission can be minimized by applying metal layer at the bottom with thickness much higher than its skin depth in the operating frequency range. Thus, throughout this study we are not dealing with the transmission as it is blocked by the metallic ground plate and the absorption equation reduced to $A(\omega) = 1 - R(\omega)$. This technique is known as coupled-system [105].

The proposed MTM absorber structure presented in Figure 6-1 comprises of three layers; aluminum ground plate at the bottom of the structure with the thickness "*h*" to prevent transmission, semiconducting layer of (5,4) SWNT with the thickness "*d*", and aluminum resonator at the surface of the semiconductor with thickness "*w*". Semiconducting layer is coupled with ground plate and the resonator to enhance the absorption of EM radiations. Algorithm based on Nicolson-Rose-Weir (NRW) approach is developed and used to obtained the material properties such as $\varepsilon(\omega)$ and $\mu(\omega)$ of the (5,4) SWNT [106]. Experimental data of (5,4) SWNT to be utilized in the algorithm is taken from a previous research [107]. All metal layers are selected to be aluminum due to its low cost, high temperature resistance, maximum reflection, and lower skin depth compared to other metals so that less material will be required, and hence the cost is reduced [100]. The frequency dependent optical properties of the aluminum can be found in Palik's studies [108]. The geometric configuration of the resonator consists of two pairs of the quadruplet patches; one quadruplet is the corner patches and the other quadruplet is at distance "a" from the center. The arrangement, orientation, and dimensions of the resonator are achieved by the optimization process that brings uniqueness to the structure and provide maximum absorption as each absorption peak is associated with

the resonant frequency of each patch. The absorption behavior of each resonator with their subsequent peaks are discussed in Section 3 in detail. It is essential to select the lateral dimension ($h + d + w$) of the whole structure smaller than the operating wavelength [109]–[111].

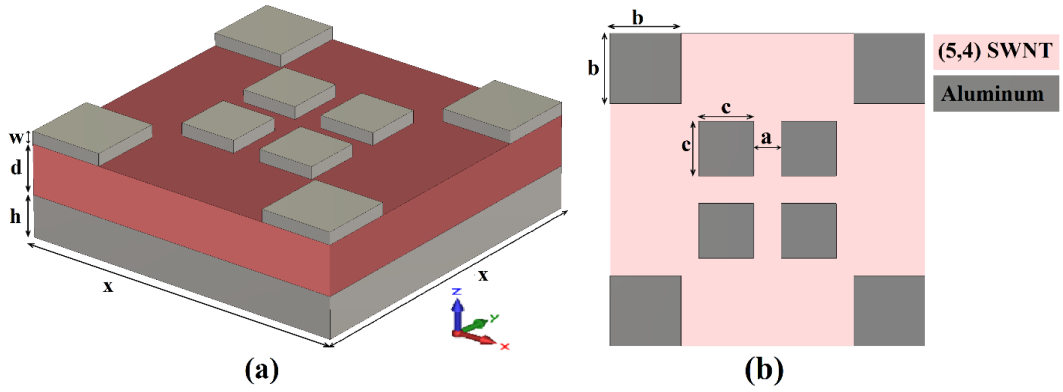

Figure 6-1: (a) Isometric view of unit-cell and dimensions associated with the proposed MTM absorber design (b) Top view of the MTM absorber design based on patch resonators.

Table 6-1: Geometrical dimensions of the proposed absorber design.

Parameter	*a*	*b*	*c*	*d*	*h*	*w*	*x*
Value (nm)	35	90	70	60	50	15	400

Full-wave EM Solver based on finite integration methods is used to analyze the absorption behavior of the proposed MTM absorber. The incident EM waves are selected to be polarized in way that e-field (x-plane) and h-field (y-plane) propagate parallel to the geometric structure, while k-vector is perpendicular to the geometric plane. Periodic boundary conditions (BCs) are specified in x and y directions and open boundaries in z-plane. Normal incident with transverse electromagnetic (TEM) wave mode is designated for all simulations unless stated that the mode of the propagation is transverse electric (TE) or transverse magnetic (TM).

6.3 Results and Discussion

Two separate but interdependent mechanisms are accountable for the resonant transmission. Firstly, excitation of surface plasmon polaritons (SPP) caused by the periodic arrangement of subwavelength structure, which can be directly affected by the arrangement and thickness of the semiconducting layer. Secondly, localized surface plasmon resonances (LSPR) caused by the shape and size of the structure. The reflection and absorption results from our simulations

are presented in Figure 6-2. Maximum absorption peaks obtained are 99.75% at 479.4 THz, 99.94% at 766.9 THz, and 97.33% at 938.8 THz. The skin depth (δ) at each resonance frequency is also calculated by Equation (6.3)

$$\delta = \frac{c}{\omega \times \tilde{k}(\omega)} \tag{6.3}$$

where, c is the speed of light, ω is the angular frequency, $\tilde{k}$ is the imaginary part of the refractive index taken from the Palik's Studies. The calculated skin depth are 13.0 nm, 12.8 nm, and 12.9 nm at resonant frequencies 479.4 THz, 766.9 THz, and 938.8 THz, respectively, which are compared with thickness of the ground metallic plate (50nm). The thickness of the metal layer is much greater than the sin depth, therefore, more than 99% of the non-transmitted EM waves are absorbed by the MTM absorber.

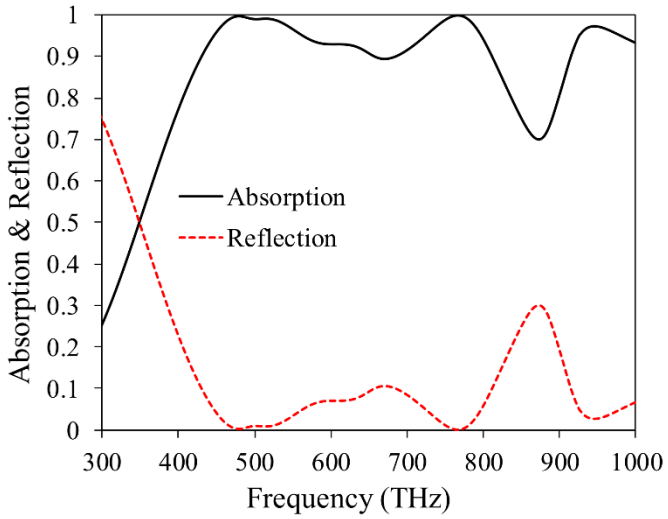

Figure 6-2: Simulated absorption and reflection results of the triple-band MTM absorber in the visible and UV range.

The strong coupling between top resonator and bottom metallic plate, which causes magnetic resonance depending on the dielectric constant of the semiconducting layer, is responsible for having maximum absorption peaks at resonant frequencies. In order to investigate the formation mechanism of the proposed MTM absorber design deeper, we divided the structure into two nanostructures. First part consists of square quadruplet patches at the corners, and the second part consists of square quadruplet patches near the center as shown in Figure 6-3 with their subsequent absorption behavior. First nanostructure provides two absorption peaks, one in the visible region (broad-band) and another in the ultraviolet region (narrow-band) with

nearly unity absorption. Second nanostructure is also responsible for the dual-band absorption but both peaks are in the ultraviolet region and provide narrow peaks. However, when both the quadruplets are combined, they provide maximum absorption with a very broad area due to strong coupling and surface plasmon effect of the resonances.

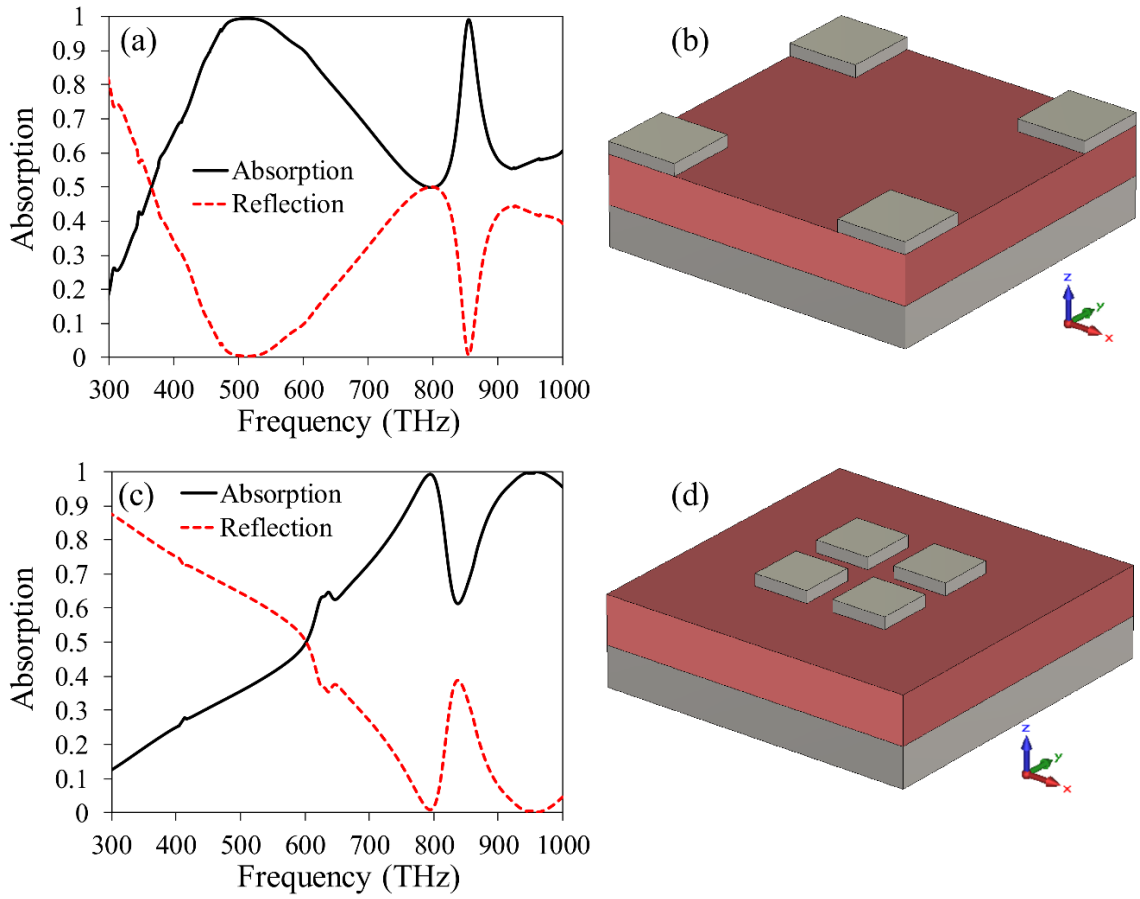

Figure 6-3: Contribution of the resonators to the proposed design (a) absorption rate of the corner quadruplet patches (b) Isometric view of unit-cell with outer quadruplet (c) Absorption rate of the inner quadruplet patches (d) Isometric view of unit-cell with inner quadruplet (b) Absorption rate of the inner quadruplet patches.

To further investigate the dependence of geometric parameters on the absorption mechanism of the MTM absorber, parametric study is conducted and simulation results of varying geometric parameters are shown in Figure 6-4. Selected results are represented by black color in all the plots. First, the effect of the periodicity on the absorption behavior is examined by altering the dimension of "x" by keeping other parameters constant. Simulated absorption results at different structural periodicity are shown in Figure 6-4(a). The dimension of the period is increased and decreased from 400nm at 10 nm intervals. When x is less than 400 nm, red shift is observed between 400 THz to 850 THz with almost the same absorption rate

as 400nm; however, blue shift is observed when x is greater than 400nm in the same frequency range. This is exactly opposite case in the frequency range of 850 to 1000 THz. This assessment is valuable for the proposed MTM absorber, which retain the absorption rate almost constant for the different values of "x" design period.

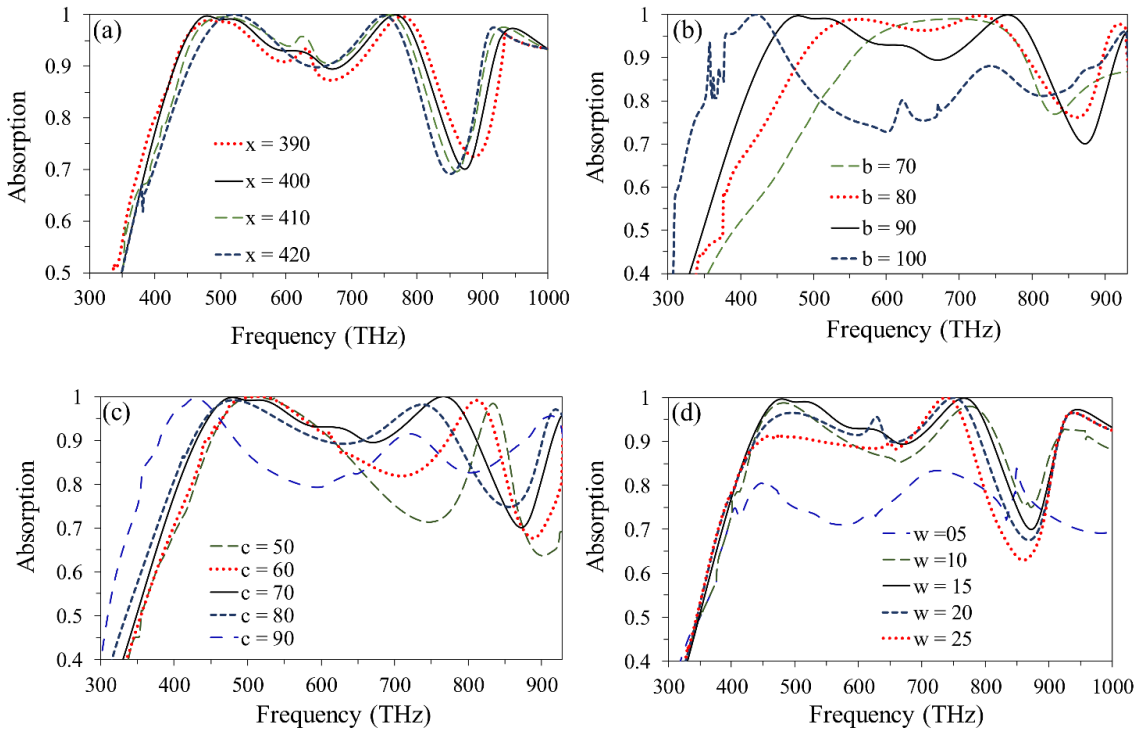

Figure 6-4: Absorption results for the parametric study (a) periodicity of the unit-cell "*x*", (b) width of the corner quadruplet patches "*b*", (c) width of the inner quadruplet patches "*c*", and (d) thickness of all patch resonators "*w*".

Secondly, absorption rate of the proposed MTM absorber is highly sensitive to the resonator's dimensions at the top of the dielectric spacer which significantly affect the absorption behavior, as confirmed by varying quadruplet patches' geometric parameters reported in Figure 6-4(b) and Figure 6-4(c). In Figure 6-4(b), corner quadruplets' dimension "b" is altered by increasing and decreasing from 90nm with the step width of 10nm. One can observe red-shift with minimum rate of absorption when the dimension of the corner quadruplets is increased from 90nm, while blue-shift with maximum absorption reached with all smaller values of "*b*". As discussed in earlier section, corner quadruplet patches are responsible for two absorption peaks, one in the visible region (broad-band) and another in the ultraviolet region (narrow-band) with nearly unity absorption. In addition to the corner quadruplet patches, the dimensions of the inner quadruplet patches also determine the absorption peaks and strength as shown in Figure 6-4(c). Results are obtained by changing the dimension with

10nm interval. Red-shift with decreased in absorption magnitude is witnessed with less than 70nm patch width. However, when width increased from 70nm, red shift with decrease absorption rate is seen. This condition is due to the interaction between resonators with the bottom metallic layer, whereby, adjusting the dimensions of the inner and outer quadruplets can have assured the multiple-band with maximum absorption.

Finally, thickness of the metallic quadruplet resonators "*w*" is one of most considerable parameters which determines the absorption strength and the positon of the resonant frequency. The variation in the resonator thickness can be seen in Figure 6-4(d). When the thin resonator of 5nm is used, magnitude of absorption is too small, less than 80% between 400 THz to 800 THz with only two absorption peaks, while third peak at 938 THz is diminished, as 5nm thickness is not sufficient to generate high absorption response. Maximum absorption with three broad peaks and higher magnitude is obtained at 15nm thickness, whereas, more than 15 nm thickness provides blue-shift with decrease in magnitude of absorption as the metallic resonators turn to behave like an optical mirror at higher thickness. Therefore, 15nm is selected to have the maximum absorption that provide near perfect coordination between reflected and transmitted radiations.

Electric field, magnetic field, and current distribution for the main three resonant frequencies of 479.8 THz, 766.9 THz and 938.8 THz are shown in Figure 6-5, Figure 6-6, and Figure 6-7, respectively. These fields and current distributions have the potential to provide complete understanding of the operating mechanism of the MTM absorber design. The resonance frequency at 479.8 THz is mainly contributed by the corner quadruplet patch as shown in Figure 6-5(a). As discussed earlier in Figure 6-3(a), the first resonance is mainly due to the contribution of the outer quadruplet. The strong electric-field is concentrated around the inner edges of the outer quadruplet patch whereas magnetic field is localized around outside of the corner patches and the dielectric layer. The concentrated e-field isolated the opposed charges which generated strong coupling between bottom metallic plate and the corner quadruplet patch. Circulating current produced around the inner side of the corner patches appears to be a result of the coupling which assisted to form magnetic response presented in Figure 6-7(a). At resonance frequency 766.9 THz, e-field is intensive completely on the central quadruplet, dielectric surface around it and the inner side of the corner patches. This resonance frequency is due to both outer and inner quadruplets which is illustrated before in Figure 6-3(a) and Figure 6-3(b), now it is evident from the Figure 6-5(b). However, magnetic field is not strong at the inner quadruplet, it is only localized around the outer quadruplet. The parallel and antiparallel surface charges circulated at the patches and more intensely towards the central

quadruplet. Electric responses are mainly controlled by parallel charges although circulating current is responsible for the magnetic response.

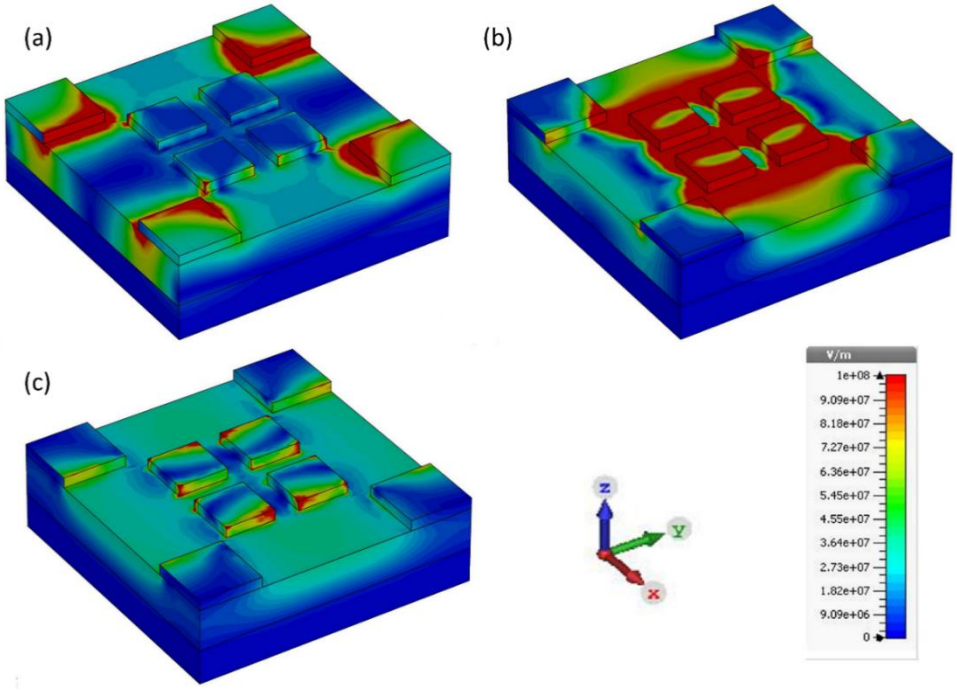

Figure 6-5: E-field distribution of the MTM absorber at the resonance frequencies (a) 479.8 THz, (b) 766.9THz, and (c) 938.8 THz.

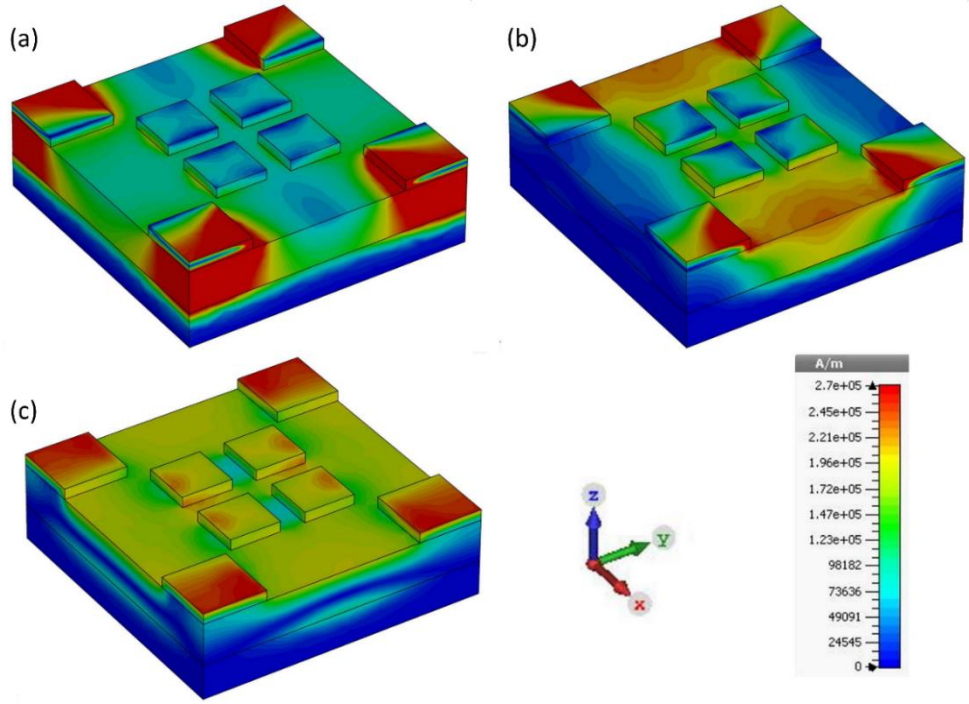

Figure 6-6: H-field distribution of the MTM absorber at the resonance frequencies (a) 479.8 THz, (b) 766.9THz, and (c) 938.8 THz.

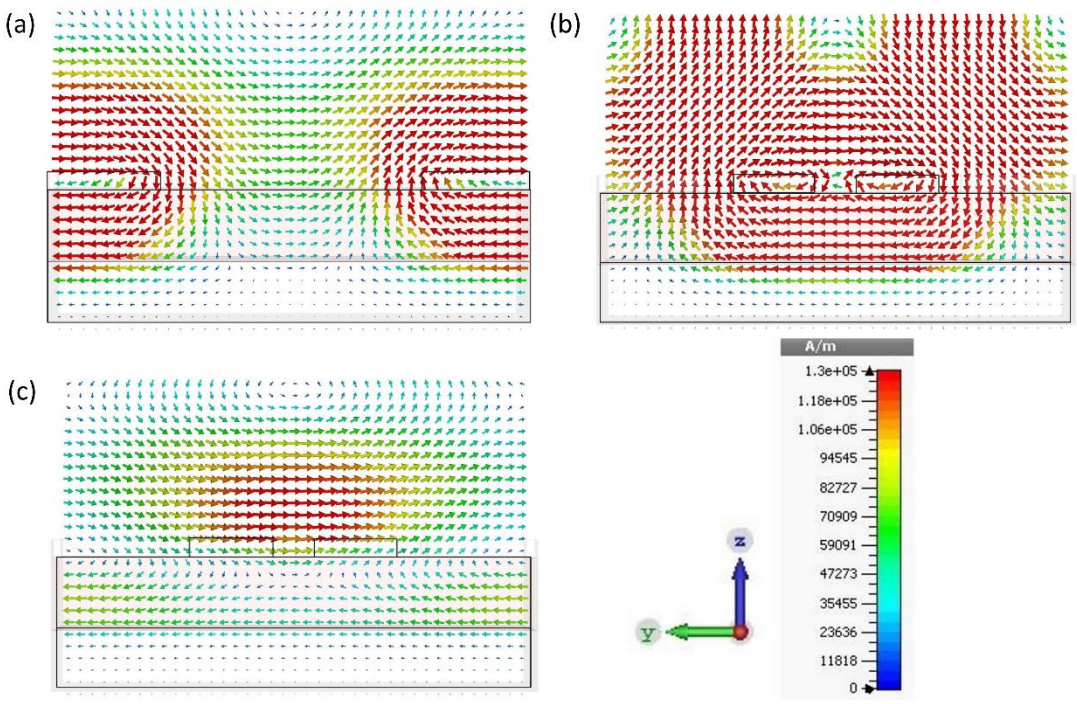

Figure 6-7: Surface current distribution of the MTM absorber at the resonance frequencies (a) 479.8 THz, (b) 766.9THz, and (c) 938.8 THz.

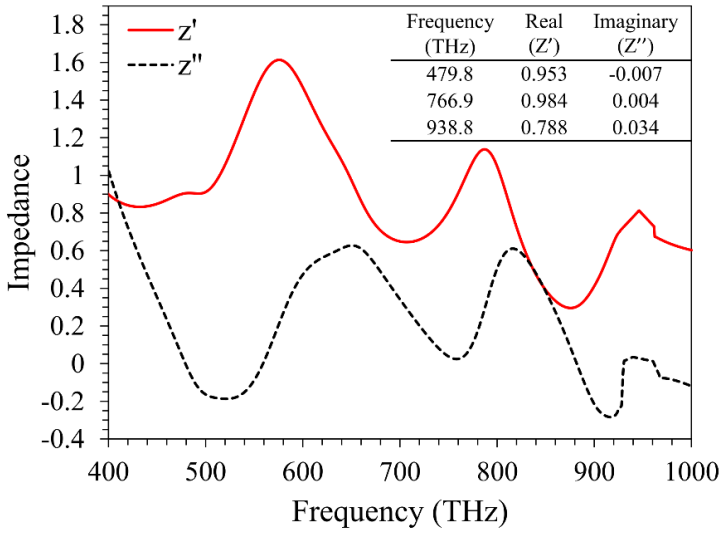

Figure 6-8: Real and imaginary parts of the relative wave impedance. The table inside provide the values of the impedance at resonance frequency.

For the third resonance frequency at 938.8 THz, the e-field and h-field is relatively lower, only a smaller portion of the central quadruplet is contributing to the electric field and the surface of the outer quadruplet is responsible for the magnetic field. Although electric and

magnetic coupling are the origin of the strong surface current, responsive surface current is also not intense. Originated e-field, h-field and current distribution are the evidences of having the same impedance of the structure as the free-space which led to achieve almost perfect - nearly equal to one - absorption rate [112]. The relative impedance of the MTM absorber is also calculated and given in Figure 6-8. The real (Z') and imaginary (Z'') part of the impedance at resonance frequencies is shown inside the Figure 6-8 as table. As can be seen from the Figure 6-8, at resonance frequencies real (Z') is almost equal to 1 and imaginary (Z'') is almost equal to zero, which ensure the impedance matching of the MTM absorber with the free-space [75]. Finally, the proposed MTM absorber is also investigated for different polarization angles (θ) under normal incident angles as shown in Figure 6-9. Polarization insensitivity and larger angle of incident radiations are very crucial parameters for real applications. In some conditions, mostly usable light cover randomly polarized components. Incident waves change their direction in x-y plane, where excited radiations are not always normally incident. To observe the behavior of polarization angle on the rate of absorption, θ is changed from 0 to 90 degrees with a step width of 30 degrees. It can be observed from the Figure 6-9 that the proposed MTM absorber is polarization insensitive under TEM mode due to the four-fold symmetry in the design.

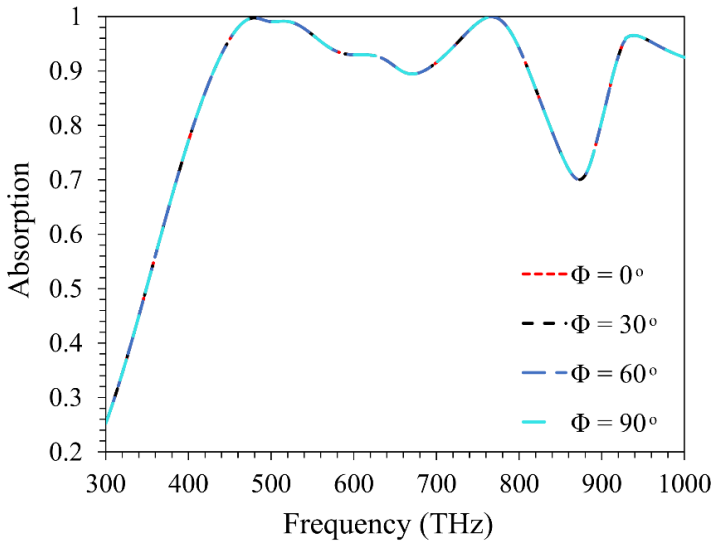

Figure 6-9: Absorption results of different polarization angles under normal incidence (TEM).

6.4 Conclusions

A triple-band polarization-insensitive MTM absorber structure is numerically simulated in the visible and ultraviolet regimes. Different possible conditions in the geometrical design are

measured to achieve maximum absorption rate. The resonant frequencies of the proposed structure can be dynamically modified by altering the intensity of the incident light. The frequency response of the absorber design offers nearly unity (99.75% at 479.4 THz, 99.94% at 766.9 THz, and 97.33% at 938.8 THz) absorption which ensued by the strong EM waves generated from the strong coupling between the patch resonator with SWNT-dielectric spacer and bottom ground metal. Further investigation is carried out to completely understand the physical mechanism of the MTM absorber design where electric-field, magnetic-field and surface current distribution of the design are discussed in details. Polarization angle is changed from 0 to 90 degrees with a step width of 30 degrees. It is observed that the proposed MTM absorber is polarization insensitive under TEM mode due to the four-fold symmetry in the design. Thus, solar cells based on this metamaterial absorber can offer nearly perfect absorption in the suggested frequency regions. The simple configuration of the design provides flexibility to control geometric parameters to be used in the solar cell and can be rescaled for other solar spectrums.

CHAPTER 7

MULTI-BAND (9,4) CHIRAL SWNT BASED METAMATERIAL

7.1 Introduction

The emerging metamaterial technology has shown the ability to perfectly absorb the solar irradiance and improvement in the efficiency of solar cells [113]. Smith et al. [114] established the synthetic materials to show the extraordinary characteristics that are not available in nature, named metamaterials. Several studies have reported MTM absorber that can perfectly absorb with single, dual, multiple, and wide band [115]–[119]. However, most of the presented structures have the limited operating frequency range, which restricts their application [120]–[123]. A MTM absorber structure operating in a broad frequency range will provide more opportunities for the solar cell to be highly efficient.

Multi-band polarization insensitive SWNT based MTM absorber is proposed in the paper that can absorb near unity in the visible and ultraviolet regimes from 300 THz to 1000 THz. The proposed design is selected due to the simplicity of the design, ease of the fabrication and the ability to absorb perfectly under changing geometry variables. The sensitivity of the polarization angle of the MTM absorber has also been investigated, which verifies that the current design is insensitive the different polarization angles. The flexibility of the proposed design by altering the geometrical components, materials, and the dimensions have also investigated, and it is confirmed that the proposed MTM absorber design provides high absorption rate under all circumstances.

7.2 Material and design

The proposed MTM absorber structure based on carbon nanotube is presented in Figure 7-1. The unit cell of the MTM with a period of *"x"* comprises of three elements; aluminum substrate with the thickness *"h"* work as a metallic mirror to prevent transmission losses, single-walled carbon nanotube (SWNT) cylindrical array, and silicon host. SWNTs are made of 15 x 15 cylindrical array with a radius *"r"* and distance between tubes *"d"* is embedded in a silicon host. Silicon host shapes a cube with a height *"l"* and width *"y"*. Unit cell characterization is done using numerical based simulation software, which is highly capable of solving Maxwell's equations, it is being reliable of producing accurate results, and suitable for high frequency and three dimensional electromagnetic structure [124], [125]. To simulate

a MTM absorber in a finite integration simulator, frequency dependent electrical properties of aluminum and silicon is extracted from Palik's studies [87]. While the frequency dependent permittivity and permeability of the (9,4) SWNT is calculated using Nicolson-Rose weir approach. Metallic ground plane is selected as aluminum due to its excellent absorption and reflection characteristics. Furthermore, aluminum is the capable of holding high temperature, and require lower material thickness due to its lower skin depth compared to other metals [100]. Silicon semiconductor is being used as the host material to make composite with the SWNTs because of its high electron mobility, capable of extreme temperatures resistance and having direct bandgap, which makes it good absorbing material. The maximum absorption and the formation of multi-band is achieved due to the unique arrangement of the nanotube by changing the distance between nanotubes and radius of the SWNTs. Polarization of EM wave in the simulation is selected in such a way that electric and magnetic fields are parallel to the incident waves, whereas, the propagation vector *k* is perpendicular to the geometric plane. Appropriate boundary conditions, periodic in *x* and *y-direction* and open add space is selected in *z-direction*. The lateral dimensions of the proposed structure should be less than the wavelength of the incident waves, so that the thickness of the MTM absorber is selected much less than the wavelength under investigation [126]–[128].

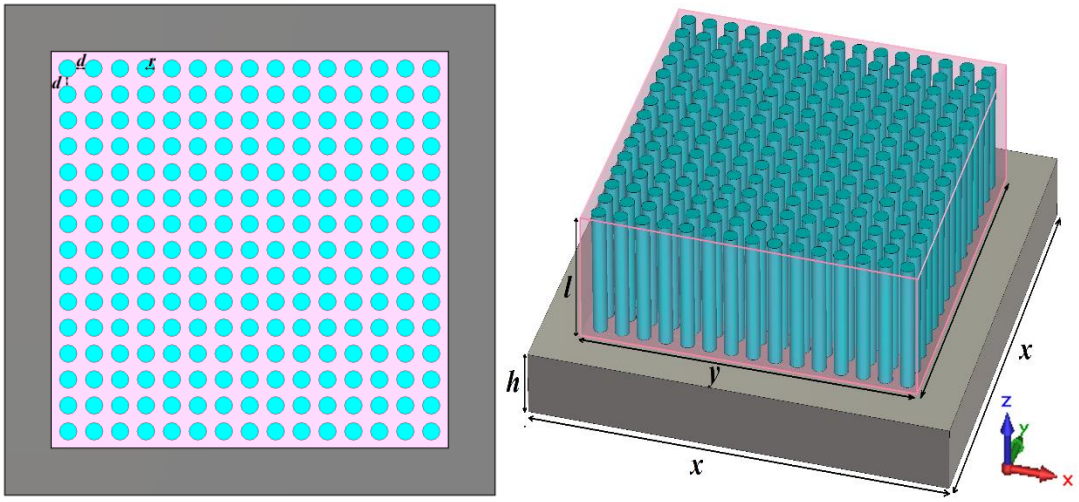

Figure 7-1: (a) Top view of the MTM absorber design based carbon nanotube wires. (b) Isometric view of unit-cell and dimensions associated with the proposed MTM absorber design made of carbon nanotubes embedded in silicon host.

Table 7-1: Geometrical dimensions of the proposed absorber design.

Parameter	*d*	*h*	*l*	*r*	*x*	*y*
Value (nm)	07	50	100	07	400	320

7.3 Results and discussion

Frequency dependent absorption $A(\omega)$ response of the MTM absorber defined by two fundamental elements; frequency dependent transmission $T(\omega)$ and frequency dependent reflection $R(\omega)$, which can be described by $A(\omega) = 1 - T(\omega) - R(\omega)$. These parameters alternatively reliant on the scattering parameters; $T(\omega) = |S_{12}|^2$ and $R(\omega) = |S_{11}|^2$. To improve the absorption characteristics of the MTM absorber, transmittance and the reflectance parameters should decreased to minimum value. To achieve this objective, the main technique used in this MTM absorber is the use of vertical SWNT composited with the silicon dielectric material. Therefore, optimization of the geometrical parameters led to the establishment of impedance matching. Free space impedance matched with the absorber's impedance, which remarkably reduced the reflection from the structure. Similarly, transmission of the structure is blocked by the metallic ground plate thickness more than the skin depth and thus achieved the zero transmission of the MTM absorber structure.

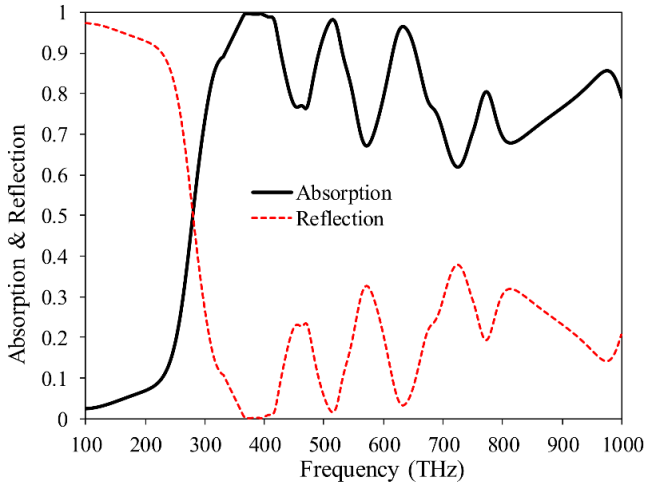

Figure 7-2: Simulated absorption and reflection spectra of the multi-band MTM absorber in the visible and UV range.

In Figure 7-2, simulated absorption and reflection spectra of the multi-band MTM absorber in the visible and UV range is presented. Four maximum absorption peaks are obtained at 394.3 THz, 514.9 THz, 632.8 THz, and 773.2 THz with the corresponding absorption rate of 99.8%, 98.35%, 96.66%, and 80.60% respectively. To understand the mechanism of the vertical nanotubes in the structure, the absorption spectra without nanotube is also presented in Figure 7-3, which only comprises of bottom aluminum metallic plate and the silicon dielectric layer. In the Figure 7-3, there are three peaks which corresponds to the same position as shown in Figure 7-2, however the absorption rate of these peaks are not as maximum as

achieved with nanotubes. In Figure 7-2, the resonances at 394.3 THz, 514.9 THz, 632.8 THz, and 773.2 THz are enhanced to the maximum near unity absorption rate by using vertical nanotubes composited with the silicon dielectric material. The first absorption peak was almost 15% without the nanotubes, which reached to the absorption rate of 99.8% with much more wider area of the peak. This is because, nanotubes create strong electric field and modifies the permittivity of the proposed MTM structure. In addition, combination between the nanotube and the silicon dielectric material make stronger magnetic field, which yield enhancement in the resonant frequencies.

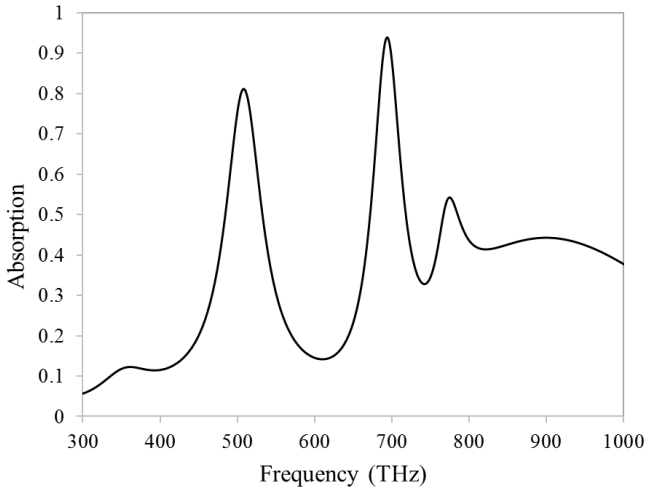

Figure 7-3: Simulated absorption spectra of the without nanotubes (only bottom metallic plate and dielectric layer of silicon)

Electric permittivity and magnetic permeability have a great influence on the properties of the absorber structure design, which can be affected by the geometrical properties of the MTM absorber. Therefore, it is important to investigate the influence of these geometrical parameters on the absorption rate. Figure 7-4Figure 7-4 (a) and (b) demonstrate the effect of the nanotube radius *"r"* and width of the silicon dielectric host *"y"*. First, the MTM structure is numerically simulated for the different values of the radius between 5 nm to 8 nm with an increment of 1 nm. The absorption rate of the MTM remains high till 7 nm but at r = 8 nm second and fourth peaks are diminishing can be seen from the Figure 7.4 (a). Also, at r = 5 nm and 6 nm peaks are narrow and not as high as at 7 nm radius, so that radius of 7 nm is selected as best. Second, the influence of dielectric host width *"y"* on the absorptivity in analyzed. The host width increased and decrease from y = 320 nm with an interval of 20 nm. In all cases, the position of the peak remains same but the rate of absorption increased and decreased. The proposed MTM design is highly sensitive to the width of the host where highest absorption rate is achieved at y = 320 nm. In Figure 7-5, absorption behavior of the

MTM at different polarization angle for normal incidence angle is demonstrated. Polarization angle is considered as the angle variation on x-y plane for the incident wave. At 90^0 angle, it refers to the E-field component of polarization wave rotating on x-y plane. Polarization angle changed from 0 to 90 degree with 30 degree interval. Perfect near unity absorption is achieved at all polarization angle, which confirms that the proposed MTM absorber structure is polarization insensitive.

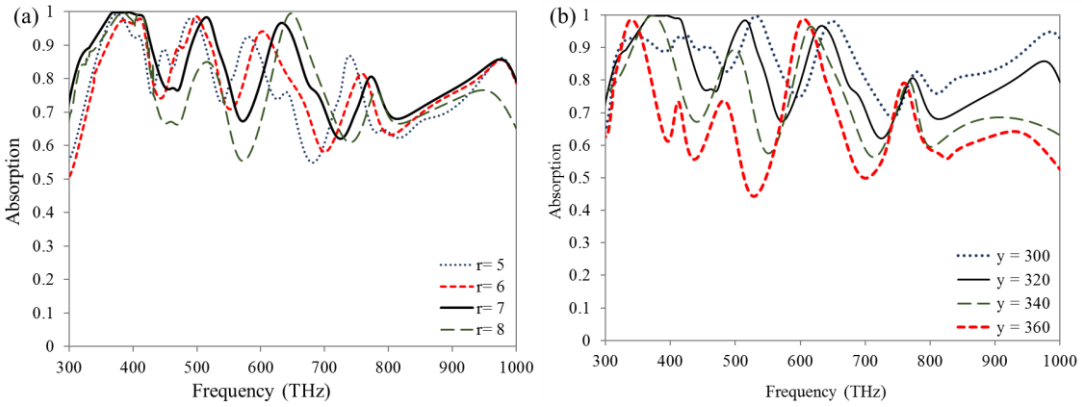

Figure 7-4: (a) Absorption results for the parametric study (a) radius of the nanotube "*r*", (b) width of the host dielectric silicon "*y*"

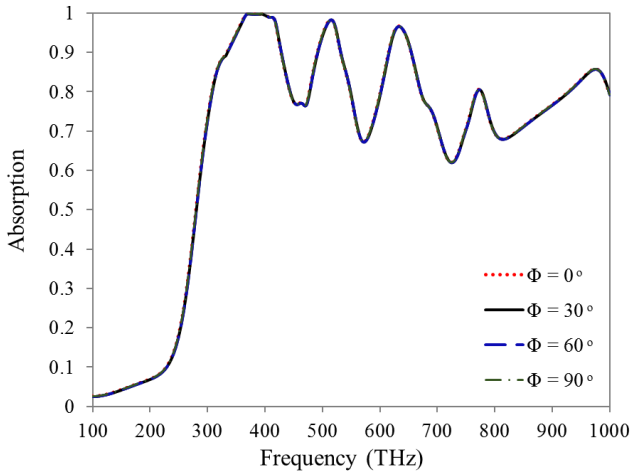

Figure 7-5: Absorption results of different polarization angles under normal incidence (TEM)

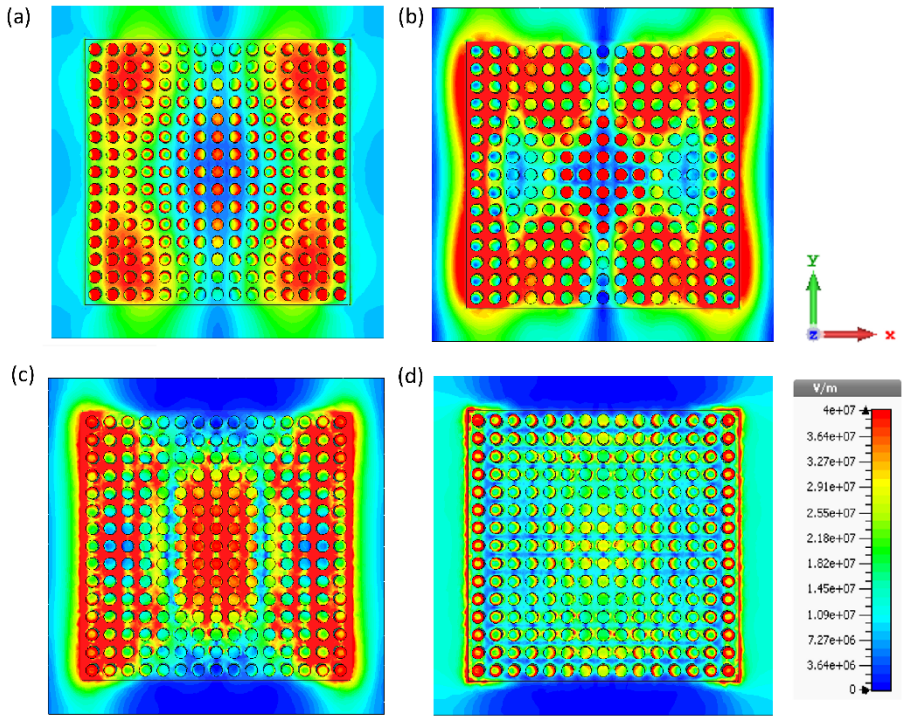

Figure 7-6: E-field distribution of the MTM absorber at the resonance frequencies (a) 393.4 THz, (b) 514.9 THz, (c) 632.8 THz, and (d) 773.2 THz.

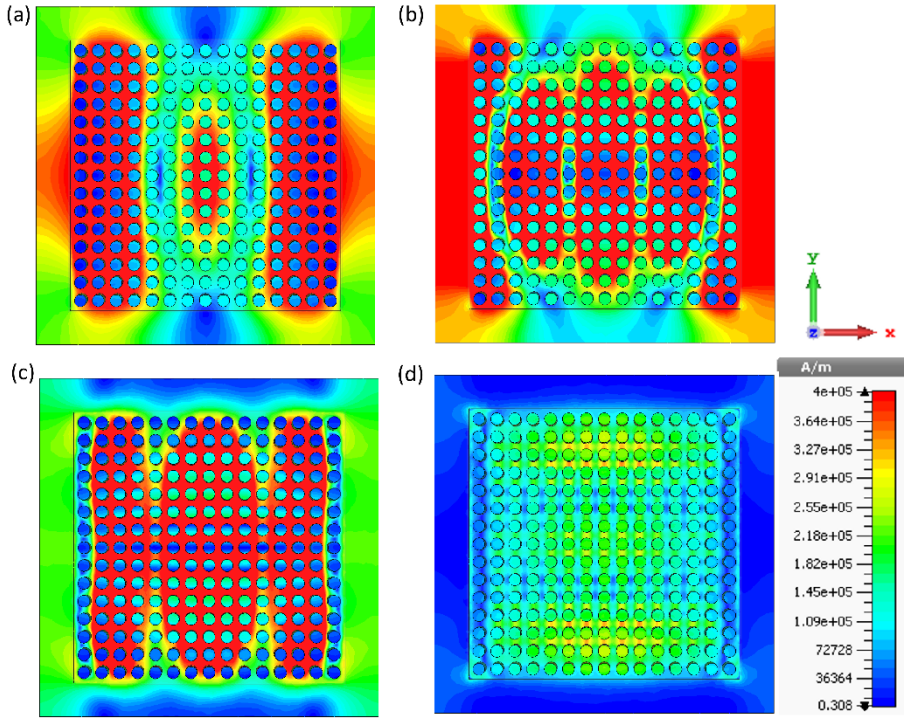

Figure 7-7: H-field distribution of the MTM absorber at the resonance frequencies (a) 393.4 THz, (b) 514.9 THz, (c) 632.8 THz, and (d) 773.2 THz.

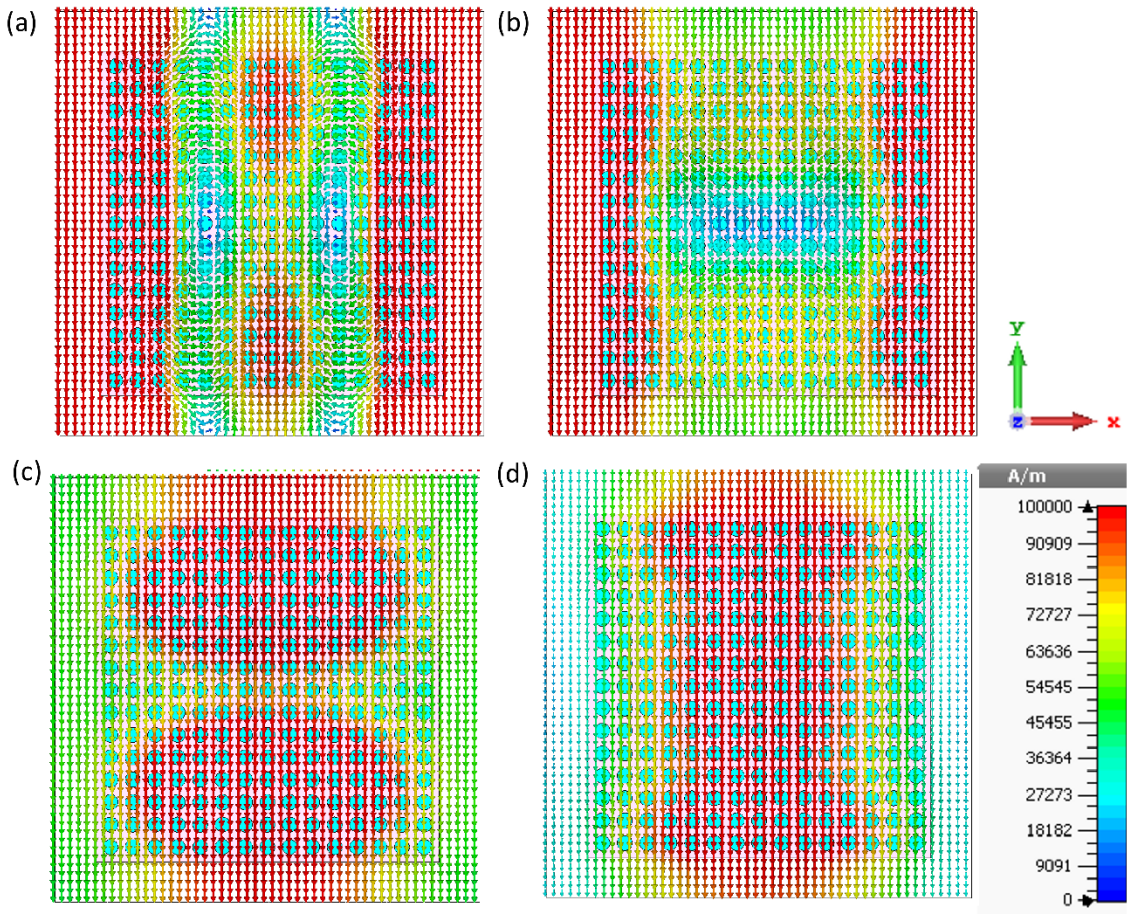

Figure 7-8: Surface current distribution of the MTM absorber at the resonance frequencies (a) 393.4 THz, (b) 514.9 THz, (c) 632.8 THz, and (d) 773.2 THz.

7.4 Conclusions

A novel multiband MTM absorber structure is based on the vertical nanotubes composited with the silicon dielectric material. Multiband polarization insensitive achieved through the unique geometrical configuration of the design, which provide almost unity absorption in the visible and ultraviolet region.

CHAPTER 8

CONCLUSIONS AND FUTURE WORK

8.1 Conclusions

Solar cells can reach high efficiencies, but their production cost is very high. Compromise between cost and efficiency is still a huge barrier for commercializing the solar cells. Therefore, it appears to be a challenging but an essential task to research and generate alternative materials. Emerging nanotechnologies have revealed carbon nanotubes (CNTs) as one of the best potential materials investigated, yet. Considering the outstanding physical, mechanical, electrochemical, thermal, and optoelectronic properties of CNTs, extensive studies have been reported assessing their applications in several disciplines. Carbon nanotube based solar cells have experienced substantial growth during the last two decades. It is the potential organic material to fulfill this challenge, which can combine different chiralities and bandgaps to get a continuous response over a wide spectrum. As discussed in chapter two, improvement in the absorption capability of the solar cell will lead to enhance the efficiency. For this purpose, various SWNT based MTM absorber with almost 99% absorption capability have been designed and numerically simulated for the solar cell application. The compact structure and maximum absorption of MTM absorber can provide highly efficient and cost effective solar cell.

The first novel MTM structure design which was the main objective of the study is discussed in chapter 5, is a wide-band (6,5) SWNT metamaterial absorber structure with near unity absorption in the visible and ultraviolet frequency. The proposed design offers wide-band with a maximum of 99.2% absorption rate caused by strong electric and magnetic fields between the strip resonator and the bottom metallic plate. The proposed design is also compared with the different chiral SWNTs. Parametric study of the proposed design is analyzed to provide the insight of absorption mechanism and to realize the effect of geometric parameters on the absorption behavior. The absorber design under investigation possesses high flexibility and is capable of keeping the wide-band with higher absorption. Moreover, an electric and magnetic field with surface current distribution is discussed in details to get the insight of the physics behind the absorption mechanism. Finally, absorption simulations are performed under the different incident and polarization angles and results are found to be polarization independent. Therefore, the proposed semiconducting (6,5) single-walled carbon

nanotube metamaterial absorber turn out to be an outstanding candidate for the maximum absorption in the visible and ultraviolet frequency regions for the solar cell application.

In chapter 6, a triple-band polarization-insensitive MTM absorber structure is numerically simulated in the visible and ultraviolet regimes. Different possible conditions in the geometrical design are measured to achieve maximum absorption rate. The resonant frequencies of the proposed structure can be dynamically modified by altering the intensity of the incident light. The frequency response of the absorber design offers nearly unity (99.75% at 479.4 THz, 99.94% at 766.9 THz, and 97.33% at 938.8 THz) absorption which ensued by the strong EM waves generated from the strong coupling between the patch resonator with SWNT-dielectric spacer and bottom ground metal. The proposed MTM absorber is polarization insensitive under TEM mode due to the four-fold symmetry in the design. Thus, solar cells based on this metamaterial absorber can offer nearly perfect absorption in the suggested frequency regions. The simple configuration of the design provides flexibility to control geometric parameters to be used in the solar cell and can be rescaled for other solar spectrums.

The last MTM absorber structure is based on the vertical nanotubes composite with the silicon dielectric material. Multiband polarization insensitive achieved through the unique geometrical configuration of the design, which provide almost unity absorption in the visible and ultraviolet region. All the MTM absorber designs proposed in this thesis are capable of improving the efficiency of the solar cell. The implementation of these MTM absorbers in the solar cells can significantly improve the absorption rate by reducing the reflection and transmission.

8.2 Future work

In this thesis, only single walled carbon nanotube (SWNT) is incorporated as a semiconducting layer in the metamaterial absorber. However, multiwalled carbon nanotube (MWNT) can also be used in the metamaterial for the future work and the comparison can be made to see the absorption capability of both SWNT and MWNT. In addition, SWNTs are used as the thin film and vertical tube composited with the other material, horizontal CNTs can be applied in the future work. The cylindrical CNTs instead of original hexagonal structure of the CNTs have been used due the limited RAM capability of the computers. It would be great if the hexagonal structure of the CNTs will be incorporated. The most important future work can be the experimental characterization and the fabrication of the proposed MTM absorbers,

BIBLIOGRAPHY

[1] M. Amouei Torkmahalleh *et al.*, "Key factors impacting performance of a salinity gradient solar pond exposed to Mediterranean climate," *Sol. Energy*, vol. 142, pp. 321–329, Jan. 2017.

[2] H. Alturaif, Z. ALOthman, J. Shapter, and S. Wabaidur, "Use of Carbon Nanotubes (CNTs) with Polymers in Solar Cells," *Molecules*, vol. 19, no. 11, pp. 17329–17344, Oct. 2014.

[3] A. R. Garfrerick, "Modeling Heterogeneous Carbon Nanotube Networks for Photovoltaic Applications Using Silvaco Atlas Software," Monterey, California. Naval Postgraduate School, 2012.

[4] R. V. Salvatierra, C. E. Cava, L. S. Roman, and A. J. G. Zarbin, "ITO-Free and Flexible Organic Photovoltaic Device Based on High Transparent and Conductive Polyaniline/Carbon Nanotube Thin Films," *Adv. Funct. Mater.*, vol. 23, no. 12, pp. 1490–1499, Mar. 2013.

[5] D. S. Hecht, L. Hu, and G. Irvin, "Emerging Transparent Electrodes Based on Thin Films of Carbon Nanotubes, Graphene, and Metallic Nanostructures," *Adv. Mater.*, vol. 23, no. 13, pp. 1482–1513, Apr. 2011.

[6] M. W. Rowell *et al.*, "Organic solar cells with carbon nanotube network electrodes," *Appl. Phys. Lett.*, vol. 88, no. 23, p. 233506, Jun. 2006.

[7] O. Hjortstam, P. Isberg, S. Söderholm, and H. Dai, "Can we achieve ultra-low resistivity in carbon nanotube-based metal composites?," *Appl. Phys. A*, vol. 78, no. 8, pp. 1175–1179, May 2004.

[8] K. D. Sattler, *Handbook of Nanophysics: Nanotubes and Nanowires*. CRC Press, 2010.

[9] M. Abdullah, F. Iskandar, and K. Okuyama, "Simple Fabrication of Carbon Nanotubes from Ethanol using an Ultrasonic Spray Pyrolysis," *J. Eng. Technol. Sci.*, vol. 36, no. 2, pp. 125–131, 2004.

[10] L. Yu, C. Shearer, and J. Shapter, "Recent Development of Carbon Nanotube Transparent Conductive Films," *Chem. Rev.*, vol. 116, no. 22, pp. 13413–13453, Nov. 2016.

[11] H. A. Alturaif, Z. A. ALOthman, J. G. Shapter, and S. M. Wabaidur, "Use of Carbon Nanotubes (CNTs) with Polymers in Solar Cells," *Molecules*, vol. 19, no. 11, pp. 17329–17344, Oct. 2014.

[12] D. O. Bellisario, R. M. Jain, Z. Ulissi, and M. S. Strano, "Deterministic modelling of carbon nanotube near-infrared solar cells," *Energy Env. Sci*, vol. 7, no. 11, pp. 3769–3781, Sep. 2014.

[13] P. J. F. Harris, “Carbon nanotube composites,” *Int. Mater. Rev.*, vol. 49, no. 1, pp. 31–43, Feb. 2004.

[14] S. Iijima and T. Ichihashi, “Single-shell carbon nanotubes of 1-nm diameter,” *Nature*, vol. 363, no. 6430, pp. 603–605, Jun. 1993.

[15] L. Wang, R. Zhou, and H. Xin, “Microwave (8 #x2013;50 GHz) Characterization of Multiwalled Carbon Nanotube Papers Using Rectangular Waveguides,” *IEEE Trans. Microw. Theory Tech.*, vol. 56, no. 2, pp. 499–506, Feb. 2008.

[16] I. Maeng, C. Kang, S. J. Oh, J.-H. Son, K. H. An, and Y. H. Lee, “Terahertz electrical and optical characteristics of double-walled carbon nanotubes and their comparison with single-walled carbon nanotubes,” *Appl. Phys. Lett.*, vol. 90, no. 5, p. 051914, Jan. 2007.

[17] S. Berciaud, L. Cognet, P. Poulin, R. B. Weisman, and B. Lounis, “Absorption Spectroscopy of Individual Single-Walled Carbon Nanotubes,” *Nano Lett.*, vol. 7, no. 5, pp. 1203–1207, May 2007.

[18] C. W. Tan, K. H. Tan, Y. T. Ong, A. R. Mohamed, S. H. S. Zein, and S. H. Tan, “Carbon Nanotubes Applications: Solar and Fuel Cells, Hydrogen Storage, Lithium Batteries, Supercapacitors, Nanocomposites, Gas, Pathogens, Dyes, Heavy Metals and Pesticides,” in *Environmental Chemistry for a Sustainable World*, E. Lichtfouse, J. Schwarzbauer, and D. Robert, Eds. Springer Netherlands, 2012, pp. 3–46.

[19] G. Miano and F. Villone, “An Integral Formulation for the Electrodynamics of Metallic Carbon Nanotubes Based on a Fluid Model,” *IEEE Trans. Antennas Propag.*, vol. 54, no. 10, pp. 2713–2724, Oct. 2006.

[20] T. A. Elwi, “A Novel Approach for Modeling the Geometry and Constitutive Parameters of an Armchair Single-Wall Carbon Nanotube Antenna Operating in the NIR Regime,” *AlMamon Univ. Coll.*, no. 24, pp. 261–285, 2014.

[21] A. E. Nikolaenko *et al.*, “Carbon Nanotubes in a Photonic Metamaterial,” *Phys. Rev. Lett.*, vol. 104, no. 15, p. 153902, Apr. 2010.

[22] P. Avouris, J. Chen, M. Freitag, V. Perebeinos, and J. C. Tsang, “Carbon nanotube optoelectronics,” *Phys. Status Solidi B*, vol. 243, no. 13, pp. 3197–3203, Nov. 2006.

[23] D. I. Odili, “Simulation and microwave measurement of the conductivity of carbon nanotubes,” PhD dissertation, University of Birmingham, 2011.

[24] K. Gharbavi and H. Badehian, “Optical properties of armchair (7, 7) single walled carbon nanotubes,” *AIP Adv.*, vol. 5, no. 7, p. 077155, Jul. 2015.

[25] E. C. Garnett, M. L. Brongersma, Y. Cui, and M. D. McGehee, “Nanowire Solar Cells,” *Annu. Rev. Mater. Res.*, vol. 41, no. 1, pp. 269–295, 2011.

[26] E. Kymakis and G. a. J. Amaratunga, “Single-wall carbon nanotube/conjugated polymer photovoltaic devices,” *Appl. Phys. Lett.*, vol. 80, no. 1, pp. 112–114, Jan. 2002.

[27] B. J. Landi, R. P. Raffaelle, S. L. Castro, and S. G. Bailey, “Single-wall carbon nanotube–polymer solar cells,” *Prog. Photovolt. Res. Appl.*, vol. 13, no. 2, pp. 165–172, Mar. 2005.

[28] R. M. Jain *et al.*, “Polymer-Free Near-Infrared Photovoltaics with Single Chirality (6,5) Semiconducting Carbon Nanotube Active Layers,” *Adv. Mater.*, vol. 24, no. 32, pp. 4436–4439, Aug. 2012.

[29] M. S. Arnold *et al.*, “Recent developments in the photophysics of single-walled carbon nanotubes for their use as active and passive material elements in thin film photovoltaics,” *Phys. Chem. Chem. Phys.*, vol. 15, no. 36, pp. 14896–14918, Aug. 2013.

[30] M.-Y. Wu, R. M. Jacobberger, and M. S. Arnold, “Design length scales for carbon nanotube photoabsorber based photovoltaic materials and devices,” *J. Appl. Phys.*, vol. 113, no. 20, p. 204504, May 2013.

[31] T. Chen *et al.*, “Flexible, Light-Weight, Ultrastrong, and Semiconductive Carbon Nanotube Fibers for a Highly Efficient Solar Cell,” *Angew. Chem. Int. Ed.*, vol. 50, no. 8, pp. 1815–1819, Feb. 2011.

[32] B. Parida, S. Iniyan, and R. Goic, “A review of solar photovoltaic technologies,” *Renew. Sustain. Energy Rev.*, vol. 15, no. 3, pp. 1625–1636, Apr. 2011.

[33] E. Klampaftis, D. Ross, K. R. McIntosh, and B. S. Richards, “Enhancing the performance of solar cells via luminescent down-shifting of the incident spectrum: A review,” *Sol. Energy Mater. Sol. Cells*, vol. 93, no. 8, pp. 1182–1194, Aug. 2009.

[34] H. A. Atwater and A. Polman, “Plasmonics for improved photovoltaic devices,” *Nat. Mater.*, vol. 9, no. 3, pp. 205–213, Mar. 2010.

[35] E. Dadrasnia, S. Puthukodan, and H. Lamela, “Terahertz electrical conductivity and optical characterization of composite nonaligned single- and multiwalled carbon nanotubes,” *J. Nanophotonics*, vol. 8, no. 1, pp. 083099–083099, 2014.

[36] V. G. Veselago, “The electrodynamics of substances with simultaneously negative values of ε and μ,” *Sov. Phys. Uspekhi*, vol. 10, no. 4, p. 509, 1968.

[37] M. A. Green, “Solar cells: operating principles, technology, and system applications,” 1982.

[38] P. RUFANGURA, “WIDE-BAND PERFECT METAMATERIAL ABSORBER FOR SOLAR CELL APPLICATIONS,” MIDDLE EAST TECHNICAL UNIVERSITY, 2015.

[39] B. G. Yacobi, *Semiconductor Materials: An Introduction to Basic Principles*. Springer Science & Business Media, 2003.

[40] Z. Ounaies, "Electrical properties of single wall carbon nanotube reinforced polyimide composites," *Compos. Sci. Technol.*, vol. 63, no. 11, pp. 1637–1646, Aug. 2003.

[41] T. W. Ebbesen, H. J. Lezec, H. Hiura, J. W. Bennett, H. F. Ghaemi, and T. Thio, "Electrical conductivity of individual carbon nanotubes," *Nature*, vol. 382, no. 6586, pp. 54–56, Jul. 1996.

[42] L. Wang, "Investigation of Carbon Nanotube Properties and Applications at Microwave and THz Frequencies," PhD dissertation, The University of Arizona., 2010.

[43] L. Nougaret *et al.*, "80 GHz field-effect transistors produced using high purity semiconducting single-walled carbon nanotubes," *Appl. Phys. Lett.*, vol. 94, no. 24, p. 243505, Jun. 2009.

[44] V. Sazonova, Y. Yaish, H. Üstünel, D. Roundy, T. A. Arias, and P. L. McEuen, "A tunable carbon nanotube electromechanical oscillator," *Nature*, vol. 431, no. 7006, pp. 284–287, Sep. 2004.

[45] R. H. Baughman, A. A. Zakhidov, and W. A. de Heer, "Carbon Nanotubes--the Route Toward Applications," *Science*, vol. 297, no. 5582, pp. 787–792, Aug. 2002.

[46] K. H. An *et al.*, "Electrochemical Properties of High-Power Supercapacitors Using Single-Walled Carbon Nanotube Electrodes," *Adv. Funct. Mater.*, vol. 11, no. 5, pp. 387–392, Oct. 2001.

[47] B. Gao *et al.*, "Electrochemical intercalation of single-walled carbon nanotubes with lithium," *Chem. Phys. Lett.*, vol. 307, no. 3–4, pp. 153–157, Jul. 1999.

[48] J. L. Kwo *et al.*, "Field emission characteristics of carbon nanotube emitters synthesized by arc discharge," *J. Vac. Sci. Technol. B*, vol. 19, no. 1, pp. 23–26, Jan. 2001.

[49] K. Masuko *et al.*, "Achievement of More Than 25 #x0025; Conversion Efficiency With Crystalline Silicon Heterojunction Solar Cell," *IEEE J. Photovolt.*, vol. 4, no. 6, pp. 1433–1435, Nov. 2014.

[50] H. Abdel Rahman, K. Kirah, H. Ghali, and W. Anis, "Simulation of carbon nanotube photovoltaic arrays," 2010, vol. 7761, p. 77610S–77610S–8.

[51] F. Dimroth *et al.*, "Wafer bonded four-junction GaInP/GaAs//GaInAsP/GaInAs concentrator solar cells with 44.7% efficiency," *Prog. Photovolt. Res. Appl.*, vol. 22, no. 3, pp. 277–282, Mar. 2014.

[52] H. A. Rahman, K. Kirah, H. Ghali, and W. Anis, "Simulation of an asymmetric contacted carbon nanotube for solar-energy harvesting," *Appl. Opt.*, vol. 53, no. 6, pp. 1237–1241, Feb. 2014.

[53] J. van de Lagemaat *et al.*, "Organic solar cells with carbon nanotubes replacing In2O3:Sn as the transparent electrode," *Appl. Phys. Lett.*, vol. 88, no. 23, p. 233503, Jun. 2006.

[54] T. M. Barnes *et al.*, "Single-wall carbon nanotube networks as a transparent back contact in CdTe solar cells," *Appl. Phys. Lett.*, vol. 90, no. 24, p. 243503, Jun. 2007.

[55] M. A. Contreras *et al.*, "Replacement of Transparent Conductive Oxides by Single-Wall Carbon Nanotubes in Cu(In,Ga)Se2-Based Solar Cells," *J. Phys. Chem. C*, vol. 111, no. 38, pp. 14045–14048, Sep. 2007.

[56] D. Stuerga, "Microwave-material interactions and dielectric properties, key ingredients for mastery of chemical microwave processes," *Microw. Org. Synth. Loupy Ed 2nd Ed Weinh. Ger. Wiley-VCH Verl. Gmbh Co KgaA*, pp. 1–61, 2006.

[57] P. Rufangura and C. Sabah, "Polarization angle insensitive dual-band perfect metamaterial absorber for solar cell applications," *Phys. Status Solidi C*, vol. 12, no. 9–11, pp. 1241–1245, Nov. 2015.

[58] M. Liang, Z. Wu, L. Chen, L. Song, P. Ajayan, and H. Xin, "Terahertz Characterization of Single-Walled Carbon Nanotube and Graphene On-Substrate Thin Films," *IEEE Trans. Microw. Theory Tech.*, vol. 59, no. 10, pp. 2719–2725, Oct. 2011.

[59] T. Chen, L. Qiu, H. Li, and H. Peng, "Polymer photovoltaic wires based on aligned carbon nanotube fibers," *J. Mater. Chem.*, vol. 22, no. 44, pp. 23655–23658, 2012.

[60] J. Yan, M. J. Uddin, T. J. Dickens, and O. I. Okoli, "Carbon nanotubes (CNTs) enrich the solar cells," *Sol. Energy*, vol. 96, pp. 239–252, Oct. 2013.

[61] M. S. Arnold *et al.*, "Broad Spectral Response Using Carbon Nanotube/Organic Semiconductor/C60 Photodetectors," *Nano Lett.*, vol. 9, no. 9, pp. 3354–3358, Sep. 2009.

[62] L. Oudjedi, A. N. G. Parra-Vasquez, A. G. Godin, L. Cognet, and B. Lounis, "Metrological Investigation of the (6,5) Carbon Nanotube Absorption Cross Section," *J. Phys. Chem. Lett.*, vol. 4, no. 9, pp. 1460–1464, May 2013.

[63] Z. Wu, L. Wang, Y. Peng, A. Young, S. Seraphin, and H. Xin, "Terahertz characterization of multi-walled carbon nanotube films," *J. Appl. Phys.*, vol. 103, no. 9, p. 094324, May 2008.

[64] T.-I. Jeon *et al.*, "Optical and electrical properties of preferentially anisotropic single-walled carbon-nanotube films in terahertz region," *J. Appl. Phys.*, vol. 95, no. 10, pp. 5736–5740, May 2004.

[65] X. Wei *et al.*, "Single-Chirality Separation and Optical Properties of (5,4) Single-Wall Carbon Nanotubes," *J. Phys. Chem. C*, vol. 120, no. 19, pp. 10705–10710, May 2016.

[66] Y. Yomogida, T. Tanaka, M. Zhang, M. Yudasaka, X. Wei, and H. Kataura, “Industrial-scale separation of high-purity single-chirality single-wall carbon nanotubes for biological imaging,” *Nat. Commun.*, vol. 7, p. 12056, Jun. 2016.

[67] L. Wang, “Investigation of Carbon Nanotube Properties and Applications at Microwave and THz Frequencies,” Jan. 2010.

[68] K. M. Lebecki, M. J. Donahue, and M. W. Gutowski, “Periodic boundary conditions for demagnetization interactions in micromagnetic simulations,” *J. Phys. Appl. Phys.*, vol. 41, no. 17, p. 175005, 2008.

[69] P. Harms, R. Mittra, and W. Ko, “Implementation of the periodic boundary condition in the finite-difference time-domain algorithm for FSS structures,” *IEEE Trans. Antennas Propag.*, vol. 42, no. 9, pp. 1317–1324, Sep. 1994.

[70] C.-P. Huang and Y.-Y. Zhu, “Plasmonics: manipulating light at the subwavelength scale,” *Act. Passive Electron. Compon.*, vol. 2007, 2007.

[71] G. A. Vandenbosch and A. Vasylchenko, *A practical guide to 3D electromagnetic software tools*. INTECH Open Access Publisher, 2011.

[72] J. Zhong, Y. Huang, G. Wen, H. Sun, P. Wang, and O. Gordon, “Single-/dual-band metamaterial absorber based on cross-circular-loop resonator with shorted stubs,” *Appl. Phys. A*, vol. 108, no. 2, pp. 329–335, 2012.

[73] L. Li, Y. Yang, and C. Liang, “A wide-angle polarization-insensitive ultra-thin metamaterial absorber with three resonant modes,” *J. Appl. Phys.*, vol. 110, no. 6, p. 063702, 2011.

[74] H. Fernández Álvarez, M. E. de Cos Gómez, and F. Las-Heras, “A six-fold symmetric metamaterial absorber,” *Materials*, vol. 8, no. 4, pp. 1590–1603, 2015.

[75] H.-T. Chen, “Interference theory of metamaterial perfect absorbers,” *Opt. Express*, vol. 20, no. 7, pp. 7165–7172, 2012.

[76] X. Shen *et al.*, “Triple-band terahertz metamaterial absorber: Design, experiment, and physical interpretation,” *Appl. Phys. Lett.*, vol. 101, no. 15, p. 154102, 2012.

[77] J. W. Park *et al.*, “Multi-band metamaterial absorber based on the arrangement of donut-type resonators,” *Opt. Express*, vol. 21, no. 8, pp. 9691–9702, 2013.

[78] T. Wanghuang, W. Chen, Y. Huang, and G. Wen, “Analysis of metamaterial absorber in normal and oblique incidence by using interference theory,” *AIP Adv.*, vol. 3, no. 10, p. 102118, 2013.

[79] F. De Nicola *et al.*, “Record efficiency of air-stable multi-walled carbon nanotube/silicon solar cells,” *Carbon*, vol. 101, pp. 226–234, May 2016.

[80] J. Lee *et al.*, “A study of mechanism on infrared photoresponse in three-dimensional single-walled carbon nanotubes,” *Carbon*, vol. 107, pp. 646–650, Oct. 2016.

[81] F. De Nicola *et al.*, "100% internal quantum efficiency in polychiral single-walled carbon nanotube bulk heterojunction/silicon solar cells," *Carbon*, vol. 114, pp. 402–410, Apr. 2017.

[82] F. De Nicola, P. Castrucci, M. Scarselli, F. Nanni, I. Cacciotti, and M. De Crescenzi, "Multi-Fractal Hierarchy of Single-Walled Carbon Nanotube Hydrophobic Coatings," *Sci. Rep.*, vol. 5, Feb. 2015.

[83] J. T. Hong *et al.*, "Dielectric Constant Engineering of Single-Walled Carbon Nanotube Films for Metamaterials and Plasmonic Devices," *J. Phys. Chem. Lett.*, vol. 4, no. 22, pp. 3950–3957, Nov. 2013.

[84] A. E. Nikolaenko, N. Papasimakis, A. Chipouline, F. D. Angelis, E. D. Fabrizio, and N. I. Zheludev, "THz bandwidth optical switching with carbon nanotube metamaterial," *Opt. Express*, vol. 20, no. 6, pp. 6068–6079, Mar. 2012.

[85] F. Rossella *et al.*, "Nanostructured magnetic metamaterials based on metal-filled carbon nanotubes," *Carbon*, vol. 96, pp. 720–728, Jan. 2016.

[86] B. Mulla and C. Sabah, "Perfect metamaterial absorber design for solar cell applications," *Waves Random Complex Media*, vol. 25, no. 3, pp. 382–392, Jul. 2015.

[87] E. D. Palik, *Handbook of Optical Constants of Solids, Five-Volume Set: Handbook of Thermo-Optic Coefficients of Optical Materials with Applications*. Academic Press, 1997.

[88] M. P. Ustunsoy and C. Sabah, "Dual-band high-frequency metamaterial absorber based on patch resonator for solar cell applications and its enhancement with graphene layers," *J. Alloys Compd.*, vol. 687, pp. 514–520, Dec. 2016.

[89] W. Zouaghi, D. Voß, M. Gorath, N. Nicoloso, and H. G. Roskos, "How good would the conductivity of graphene have to be to make single-layer-graphene metamaterials for terahertz frequencies feasible?," *Carbon*, vol. 94, pp. 301–308, Nov. 2015.

[90] P. Rufangura and C. Sabah, "Design and characterization of a dual-band perfect metamaterial absorber for solar cell applications," *J. Alloys Compd.*, vol. 671, pp. 43–50, Jun. 2016.

[91] B. Mulla and C. Sabah, "Multi-band metamaterial absorber topology for infrared frequency regime," *Phys. E Low-Dimens. Syst. Nanostructures*, vol. 86, pp. 44–51, Feb. 2017.

[92] H.-T. Chen *et al.*, "Experimental demonstration of frequency-agile terahertz metamaterials," *Nat. Photonics*, vol. 2, no. 5, pp. 295–298, May 2008.

[93] S. B. Choi *et al.*, "Nanopattern enabled terahertz all-optical switching on vanadium dioxide thin film," *Appl. Phys. Lett.*, vol. 98, no. 7, p. 071105, Feb. 2011.

[94] H.-T. Chen, W. J. Padilla, J. M. O. Zide, A. C. Gossard, A. J. Taylor, and R. D. Averitt, "Active terahertz metamaterial devices," *Nature*, vol. 444, no. 7119, pp. 597–600, Nov. 2006.

[95] J. T. Hong *et al.*, "Dielectric constant engineering of single-walled carbon nanotube films for metamaterials and plasmonic devices," *J. Phys. Chem. Lett.*, vol. 4, no. 22, pp. 3950–3957, 2013.

[96] G. B. Jung *et al.*, "Terahertz Spectroscopy of Nanocrystal−Carbon Nanotube and −Graphene Oxide Hybrid Nanostructures," *J. Phys. Chem. C*, vol. 114, no. 25, pp. 11258–11265, Jul. 2010.

[97] M. A. Seo *et al.*, "Terahertz electromagnetic interference shielding using single-walled carbon nanotube flexible films," *Appl. Phys. Lett.*, vol. 93, no. 23, p. 231905, Dec. 2008.

[98] Y. Liu, Y. Chen, J. Li, T. Hung, and J. Li, "Study of energy absorption on solar cell using metamaterials," *Sol. Energy*, vol. 86, no. 5, pp. 1586–1599, 2012.

[99] P. Rufangura and C. Sabah, "Polarization angle insensitive dual-band perfect metamaterial absorber for solar cell applications," *Phys. Status Solidi C*, vol. 12, no. 9–11, pp. 1241–1245, 2015.

[100] B. Mulla and C. Sabah, "Perfect metamaterial absorber design for solar cell applications," *Waves Random Complex Media*, vol. 25, no. 3, pp. 382–392, 2015.

[101] F. Dincer, O. Akgol, M. Karaaslan, E. Unal, and C. Sabah, "Polarization angle independent perfect metamaterial absorbers for solar cell applications in the microwave, infrared, and visible regime," *Prog. Electromagn. Res.*, vol. 144, pp. 93–101, 2014.

[102] M. Li, H.-L. Yang, X.-W. Hou, Y. Tian, and D.-Y. Hou, "Perfect metamaterial absorber with dual bands," *Prog. Electromagn. Res.*, vol. 108, pp. 37–49, 2010.

[103] B. Zhu, Z. Wang, C. Huang, Y. Feng, J. Zhao, and T. Jiang, "Polarization insensitive metamaterial absorber with wide incident angle," *Prog. Electromagn. Res.*, vol. 101, pp. 231–239, 2010.

[104] L. Huang and H. Chen, "Multi-band and polarization insensitive metamaterial absorber," *Prog. Electromagn. Res.*, vol. 113, pp. 103–110, 2011.

[105] H.-T. Chen, "Interference theory of metamaterial perfect absorbers," *Opt. Express*, vol. 20, no. 7, pp. 7165–7172, 2012.

[106] Ö. KÜÇÜKSARI, "Novel Multi-Band Metamaterials in Microwave Region With Applications In Antennas," Middle East Technical University, 2014.

[107] X. Wei *et al.*, "Single-Chirality Separation and Optical Properties of (5, 4) Single-Wall Carbon Nanotubes," *J. Phys. Chem. C*, vol. 120, no. 19, pp. 10705–10710, 2016.

[108] E. D. Palik, *Handbook of Optical Constants of Solids, Five-Volume Set: Handbook of Thermo-Optic Coefficients of Optical Materials with Applications*. Academic Press, 1997.

[109] R. Huang, Z.-W. Li, L. B. Kong, L. Liu, and S. Matitsine, "Analysis and design of an ultra-thin metamaterial absorber," *Prog. Electromagn. Res. B*, vol. 14, pp. 407–429, 2009.

[110] K. Wu, Y. Huang, T. Wanghuang, W. Chen, and G. Wen, "Numerical and theoretical analysis on the absorption properties of metasurface-based terahertz absorbers with different thicknesses," *Appl. Opt.*, vol. 54, no. 2, pp. 299–305, 2015.

[111] M. P. Ustunsoy and C. Sabah, "Dual-band high-frequency metamaterial absorber based on patch resonator for solar cell applications and its enhancement with graphene layers," *J. Alloys Compd.*, vol. 687, pp. 514–520, 2016.

[112] F. Dincer, M. Karaaslan, E. Unal, K. Delihacioglu, and C. Sabah, "Design of polarization and incident angle insensitive dual-band metamaterial absorber based on isotropic resonators," *Prog. Electromagn. Res.*, vol. 144, pp. 123–132, 2014.

[113] C. M. Watts, X. Liu, and W. J. Padilla, "Metamaterial Electromagnetic Wave Absorbers (Adv. Mater. 23/2012)," *Adv. Mater.*, vol. 24, no. 23, 2012.

[114] D. R. Smith, W. J. Padilla, D. C. Vier, S. C. Nemat-Nasser, and S. Schultz, "Composite medium with simultaneously negative permeability and permittivity," *Phys. Rev. Lett.*, vol. 84, no. 18, p. 4184, 2000.

[115] B. Bian *et al.*, "Novel triple-band polarization-insensitive wide-angle ultra-thin microwave metamaterial absorber," *J. Appl. Phys.*, vol. 114, no. 19, p. 194511, Nov. 2013.

[116] C. Gu *et al.*, "A Wide-Band, Polarization-Insensitive and Wide-Angle Terahertz Metamaterial Absorber," *Prog. Electromagn. Res. Lett.*, vol. 17, pp. 171–179, 2010.

[117] X. Liu, T. Tyler, T. Starr, A. F. Starr, N. M. Jokerst, and W. J. Padilla, "Taming the Blackbody with Infrared Metamaterials as Selective Thermal Emitters," *Phys. Rev. Lett.*, vol. 107, no. 4, p. 045901, Jul. 2011.

[118] B. Zhu, C. Huang, Y. Feng, J. Zhao, and T. Jiang, "Dual Band Switchable Metamaterial Electromagnetic Absorber," *Prog. Electromagn. Res. B*, vol. 24, pp. 121–129, 2010.

[119] B. Zhu, Z. Wang, C. Huang, Y. Feng, J. Zhao, and T. Jiang, "Polarization Insensitive Metamaterial Absorber with Wide Incident Angle," *Prog. Electromagn. Res.*, vol. 101, pp. 231–239, 2010.

[120] L. Huang and H. Chen, "Multi-Band and Polarization Insensitive Metamaterial Absorber," *Prog. Electromagn. Res.*, vol. 113, pp. 103–110, 2011.

[121] X. Shen *et al.*, “Triple-band terahertz metamaterial absorber: Design, experiment, and physical interpretation,” *Appl. Phys. Lett.*, vol. 101, no. 15, p. 154102, Oct. 2012.

[122] G.-D. Wang, J.-F. Chen, X. Hu, Z.-Q. Chen, and M. Liu, “Polarization-Insensitive Triple-Band Microwave Metamaterial Absorber Based on Rotated Square Rings,” *Prog. Electromagn. Res.*, vol. 145, pp. 175–183, 2014.

[123] X.-H. Wang, H. Zhou, M. Yan, N. Fu, M.-Y. Li, and X.-H. Wang, “A Tri-Band Electromagnetic Absorber with Insensitive Properties,” *Prog. Electromagn. Res. Lett.*, vol. 49, pp. 119–123, 2014.

[124] M. C. T. Weiland, “Discrete electromagnetism with the finite integration technique,” *Prog. Electromagn. Res.*, vol. 32, pp. 65–87, 2001.

[125] R. Marklein, “The finite integration technique as a general tool to compute acoustic, electromagnetic, elastodynamic, and coupled wave fields,” *Rev. Radio Sci.*, vol. 2002, pp. 201–244, 1999.

[126] K. Wu, Y. Huang, T. Wanghuang, W. Chen, and G. Wen, “Numerical and theoretical analysis on the absorption properties of metasurface-based terahertz absorbers with different thicknesses,” *Appl. Opt.*, vol. 54, no. 2, pp. 299–305, 2015.

[127] M. Gil, J. Bonache, and F. Martin, “Metamaterial filters: A review,” *Metamaterials*, vol. 2, no. 4, pp. 186–197, 2008.

[128] S. Walia *et al.*, “Flexible metasurfaces and metamaterials: A review of materials and fabrication processes at micro-and nano-scales,” *Appl. Phys. Rev.*, vol. 2, no. 1, p. 011303, 2015.